



Low-Frequency Observations of the Radio Sky from Marion Island

By

Tankiso H. Moso

Submitted in the School of Mathematics, Statistics and Computer Sciences
in fulfilment of the academic requirements for the
Master of Science Degree in Applied Mathematics
at the

University of Kwa-Zulu Natal, Westville Campus

Supervisor Signature
Prof. H. C. Chiang

Co-Supervisor Signature
Prof. K. Moodley

Student Signature
Tankiso H. Moso

February, 2021

Declaration - Plagiarism

I, Tankiso H. Moso, declare that

1. The research reported in this thesis, except where otherwise indicated, is my original research.
2. This thesis has not been submitted for any degree or examination at any other university.
3. This thesis does not contain the data, photographs, graphs, or other material of other persons unless expressly recognized as obtained from other people.
4. This thesis does not contain other persons' writing unless expressly recognized as having been sourced from other researchers. Where additional written sources have been cited, then:
 - (a) Their words have been re-written, but the general information attributed to them has been referenced.
 - (b) Where their exact words have been used, then their writing has been placed in italics and inside quotation marks and referenced.
5. This thesis does not contain text, graphics or tables copied and pasted from the internet unless specifically acknowledged, and the source being detailed in the thesis and the Bibliography section.

Tankiso H. Moso

Thursday 4th February, 2021

Publication List

Publications arising from the work presented in this thesis:

1. The Array of Long Baseline Antennas for Taking Radio Observations from the Sub-Antarctic [[Chiang et al., 2020](#)], and
2. Radio-Frequency Interference at the McGill Arctic Research Station [[Dyson et al., 2020](#)] has been submitted.

Abstract

Measurements of the radio sky at frequencies below \sim 100 MHz have the potential to unlock a new observational window into the universe's history. These observations allow us to probe early epochs of the universe's history and lay the groundwork for eventually exploring the "dark ages" through to the cosmic dawn. There is minimal knowledge about the radio sky below 30 MHz. The lowest measured frequency of the radio sky dated from the 1960s when Grote Reber mapped a portion of the sky at \sim 2 MHz using a 192-element dipole array with \sim 5 $^{\circ}$ resolution. This brief glimpse of low-frequency Galactic emission was made possible partly by a profound solar minimum.

This thesis presents the Array of Long Baseline Antennas for Taking Radio Observations from the Sub-Antarctic (ALBATROS) and upgrades to Probing Radio Intensity at high-Z from Marion (PRI^ZM) subsystems. ALBATROS is a new experimental effort aimed at imaging the low-frequency sky as the first step toward future mapping of the dark ages. The PRI^ZM experiment is intended to search for the feature of cosmic dawn absorption in globally averaged redshifted 21-cm emission. The two experiments are installed in Marion Island, located in the southern Indian Ocean. This thesis focuses on deploying the first autonomous ALBATROS station, which took place in 2019. Prior to the autonomous station's deployment, a two-element pathfinder was installed to assess the observable frequencies from Marion below 30 MHz. The final ALBATROS array will consist of ten autonomous antenna stations separated by maximum baseline lengths of \sim 20 km. The design of a new second stage electronics (SSE) enclosure and other subsystem upgrades for PRI^ZM that were intended for the 2020 deployment are presented in this thesis. The enclosure was revised so that each antenna is serviced by its SSE box, and more compact subsystems were designed to fit in the new box.

Preliminary observations from the ALBATROS pathfinder installed in April 2018 show discernible interferometric fringes from the sky visible down to \sim 10 MHz without any data processing or cuts. The first fully autonomous antenna station was deployed in April 2019, configured to record baseband data and solar panels' power. The first autonomous ALBATROS station is fully operational. The solar power system sufficiently charges the batteries. The hardware was successfully secured against the wind storms and mice. The preliminary low-frequency data are exceptional compared to the pathfinder observations, as we are currently experiencing a solar minimum. So far, the new solar power control electronics appear to be radio-quiet, and there is no qualitative evidence of self-generated contamination from radio-frequency noise.

Acknowledgements

Throughout my life, I have been blessed, highly favored, and fortunate to have been granted several opportunities that have led me to undertake this research thesis. Thank you to the thousands of people in the universe who have provided me with the foundation, environment, safety, health, support, service, financial well-being, love, joy, knowledge, kindness, calmness, and happiness to produce this work.

My sincerest gratitude goes to Profs. Cynthia Chiang and Jonathan Sievers for giving me a platform to realize and prove my strengths and capabilities. The unusual path that I took in joining radio astronomy research is a lifetime opportunity that has opened doors for me and my career. Words can never express my gratitude for the life skills, adventurous experiences, and independence that I have gained through you. It has indeed been a great ride!

I want to thank Prof. Matt Hilton and Dr. Ilya Sinayskiy. During the years that I have spent at the University of KwaZulu Natal, you have had a remarkable impact on my academic and career growth and recognition.

A special thanks to the National Astrophysics and Space Science Programme for funding my studies since 2018. This thesis's completion would not have been possible without collaborative efforts from the McGill University, PRI^ZM and AL-BATROS teams, and the H1-225 lab mates.

All my friends and acquaintances who have been pushing me to do and be the best I can, I thank you all for therapeutic sessions, academic, financial, personal growth, empathy, motivation, and outings.

My family's prayers throughout this journey of life have been my greatest pillar of strength. The support I receive from you, Mongi is immeasurable; thank you for always having my back.

"Dear God, thank you...!"

Table of Contents

Declaration	i
Publication List	ii
Abstract	iii
Acknowledgements	iv
1 Introduction	1
1.1 History of the Universe	1
1.2 Cosmology with Redshifted 21-cm Emission	3
1.2.1 Dark Ages	4
1.2.2 Cosmic Dawn	5
1.3 Hydrogen Line Observational Challenges	5
1.4 Previous Cosmic Dawn and Low-frequency Experiments	7
1.4.1 Global Signal Experiments for Cosmic Dawn	7
1.4.2 Imaging below 30 MHz	8
1.5 Structure of this Thesis	10
2 Observing at the Marion Island Site	12
2.1 Marion Island	12
2.2 Advantages of Observing from Marion Island	14
3 ALBATROS Experiment	18
3.1 Overview of the Pathfinder	18
3.2 Pathfinder System Signal Chain	18
3.2.1 Antenna	18
3.2.2 Front-end Electronics	20
3.2.3 Back-end Electronics	21
3.2.4 Power	23
3.3 Overview of Autonomous Stations	24
3.4 2019 Marion Voyage	24
3.5 Autonomous Station Signal Chain	26
3.5.1 Back-end Electronics	27
3.5.2 Solar Power Supply System	30
4 PRI^ZM Instrumentation	34
4.1 PRI ^Z M Experiment Overview	34
4.2 Signal Chain	34
4.2.1 Antenna	34
4.2.2 First Stage Electronics	35
4.2.3 Second Stage Electronics (SSE)	35
4.2.4 Power	39

4.3	Revised PRI ^Z M Instrumentation	39
4.3.1	First Stage Electronics (FSE)	42
4.3.2	Second Stage Electronics	43
5	Preliminary Data and Future Outlook	50
5.1	Conclusion and Future Outlook	54

Chapter 1

Introduction

Our universe's origin has always been a mystery until humankind started looking for answers to the unanswered questions about the evolution of the cosmos. The search for solutions led to a field of study called cosmology. This field has drastically impacted our knowledge of the universe's evolution [Kolb E. W, 1988].

Humans initially believed that the Sun, the moon, and other planets orbited the Earth until Nicolaus Copernicus and other astronomers replaced the geocentric model with the heliocentric model [Rabin, 2019; Kanas, 2012]. Celestial mechanics emerged as an area of study after Isaac Newton discovered that elliptical planet motion could be explained by gravitational force attraction [Rabin, 2019; Crowe, 2013]. In the modern study of the universe, our understanding of gravity has been further refined by Albert Einstein's theory of general relativity, which presents the mathematical framework required to describe the universe's evolution. The latest observations show that the universe is expanding, and the speeds of distant galaxies and their distances from Earth are proved to be directly related. The cosmic microwave background (CMB) detection is residual radiation from the time the universe began. The two observations that cemented the big bang model were the expansion of the universe and the CMB detection.

Georges Lemaitre proposed the Big Bang theory, the contemporary model that explains the universe's expansion [Hubble, 1926]. The Big Bang theory was established from Hubble's law and subsequently by Arno Penzias and Robert Wilson in 1964 from discovering the cosmic microwave background (CMB) [Penzias and Wilson, 1965; Peebles and Ratra, 2003; Hubble, 1929]. The Supernova Cosmology Project and the High-Z Supernovae Search Team in 1998 discovered the universe's acceleration using observations of type Ia supernovae [Riess et al., 1998; Perlmutter et al., 1999]. The accelerated expansion is described by dark energy, which accounts for approximately 70 percent of the universe's energy density. Today, understanding dark energy's nature is a significant area of focus in astrophysics and particle physics [Frieman et al., 2008].

1.1 History of the Universe

Figure 1.1 shows the cosmic history of the universe. The Planck era, which lasted until 10^{-43} s after the big bang, is unknown to physicists and requires a quantum theory of gravity. Following the Planck era, 10^{-34} s after the big bang, the universe went through a period of rapid exponential expansion, known as Inflation [Guth,

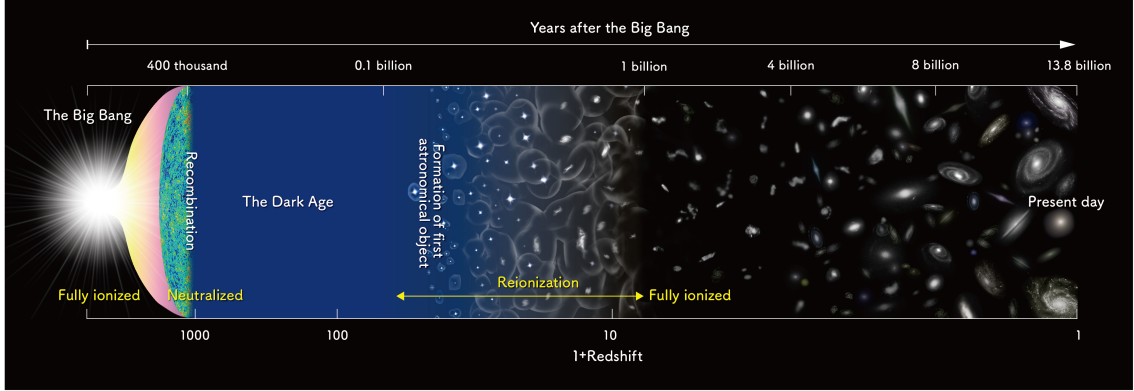


Figure 1.1: The cosmic history of the Universe from the Big Bang to its early years, through the dark ages to the epoch of reionization and the post-reionization epoch. Image credit: National Optical Astronomy Observatory

1981].

Recombination occurred when the universe cooled enough for neutral hydrogen (HI) to form, around a redshift of $z \sim 1100$. Redshift enables us to gain access to the early age of the universe, which means that the higher the redshift, the further away we can look back in time. The redshift-wavelength relation is given by

$$1 + z = \frac{\lambda_{obs}}{\lambda_{emit}} = \frac{1}{a} \quad (1.1)$$

where z is the redshift, λ_{obs} is the wavelength of the observed signal, λ_{emit} is the wavelength of the signal emitted, and a is the Universe expansion scale factor. Before recombination, electrons were not bound to protons, and the universe contained ionized plasma known as photon-baryon fluid. Decoupled photons then formed the CMB [Penzias and Wilson, 1965].

Subsequently, HI became the dominant baryonic component of the intergalactic medium (IGM) during the dark ages ($1100 \gtrsim z \gtrsim 30$). No measurements of the dark ages exist, and if hydrogen can be mapped in this era, valuable cosmological data can be produced [Lazio et al., 2016; Loeb and Zaldarriaga, 2004].

There were density fluctuations in the distribution of matter. The overdense regions collapsed under gravity's influence, ultimately creating the first stars and resulting in Cosmic Dawn ($30 \gtrsim z \gtrsim 10$). Energy from the first stars ultimately fully reionized the universe. Galaxies, galaxy clusters, and large-scale structures that exist in the present universe evolved after the first stars were born [Deng et al., 2017; Burns et al., 2012].

Throughout the cosmological epochs, what is known is minimal because it is challenging to observe them directly. The growth of 21 cm cosmology can fill the gaps in our knowledge of the universe's history [Pritchard and Loeb, 2012]. A brief overview of the universe's history has been given, and the next section will cover 21 cm cosmology corresponding to the dark ages and cosmic dawn in more detail.

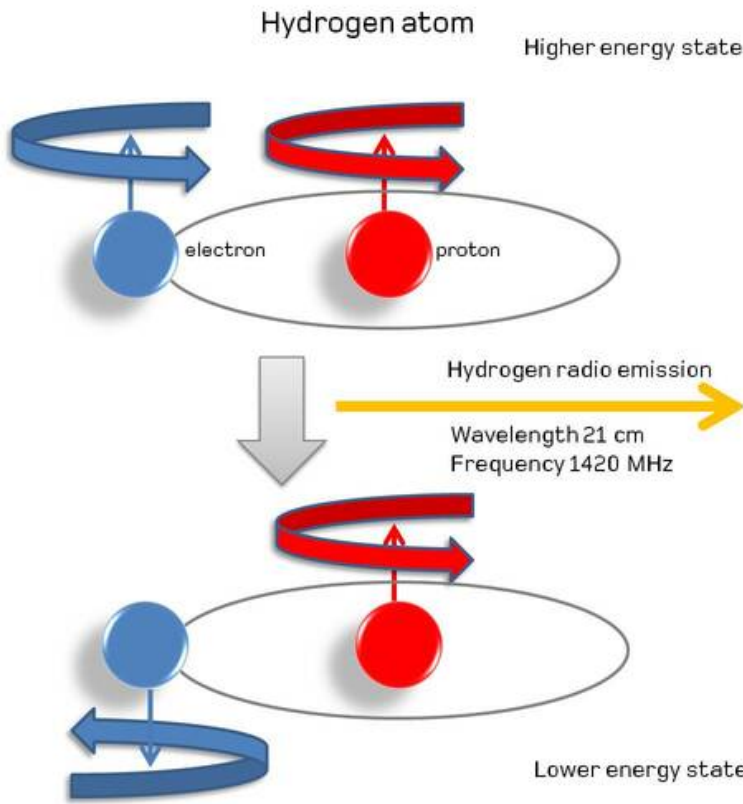


Figure 1.2: The formation of the 21 cm wavelength line by the process of the spin flip transition where the hydrogen atom moves from one energy state to another. Image credit: Square Kilometre Array.

1.2 Cosmology with Redshifted 21-cm Emission

Because hydrogen gas is the most abundant element in the universe, there is a concerted effort in the experimental community to develop telescopes for mapping neutral hydrogen via 21 cm emission. This hydrogen line is an essential mechanism for probing the dark ages to the epoch of reionization (EoR) [Liu et al., 2013; Pober et al., 2014]. The generation of the hydrogen line (21 cm line or HI line) is due to the intrinsic electron and proton spins within the hydrogen atoms [Giancoli, 2008]. The electron and proton spins can be oriented in either the opposing or the same direction, respective to each other. When the spins are opposing or antiparallel, the hydrogen atom is in the lower energy state. When the spins are parallel, the hydrogen atom is in a higher energy state. When an electron transitions from the higher energy state to the lower, the hydrogen atom discharges a photon with a 21 cm wavelength, equivalent to 1420 MHz. The hyperfine splitting of the two energy states is equivalent to $\Delta E = 5.9 \times 10^{-6}$ eV. Figure 1.2 shows the spin-flip transition process [Giancoli, 2008; Liu and Chronopoulos, 2008].

The populations of the low- and high-energy spin states, n_0 and n_1 , define the spin temperature T_s :

$$\frac{n_0}{n_1} = \frac{g_1}{g_0} e^{(-E_1 0)/k_B T_s} = 3e^{-T_* T_s}. \quad (1.2)$$

Here $\frac{g_1}{g_0} = 3$ is the spin degeneracy of the triplet and singlet levels, and $T_* \equiv hc/k$

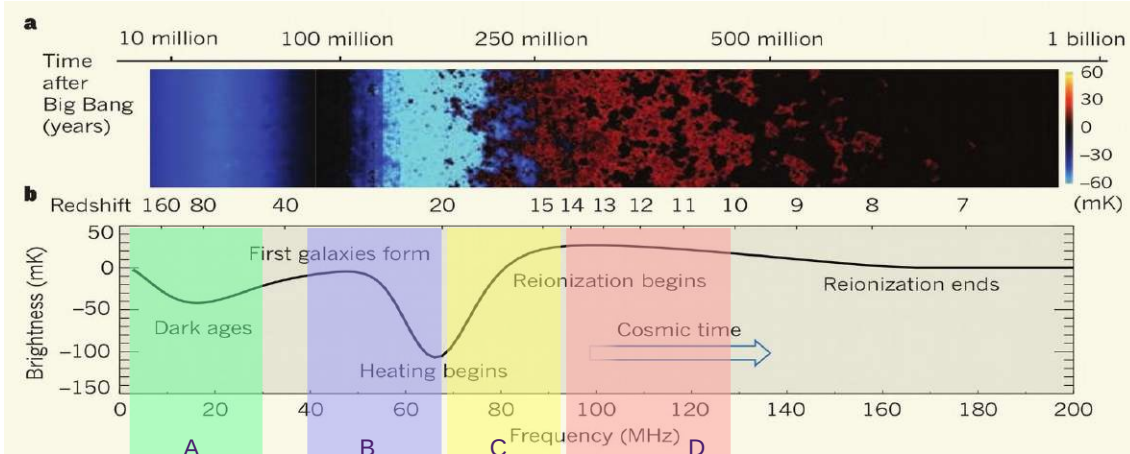


Figure 1.3: Frequency structure of the globally averaged 21 cm signal: (a) shows the spatial and temporal evolution of the 21 cm brightness temperature and (b) shows the predicted time evolution of the globally averaged 21 cm brightness temperature [Pritchard and Loeb, 2012]. There are different physical processes that govern the four highlighted (A to D) periods and the details are discussed in the main text.

$\lambda_{21cm} = 0.068$ K is the equivalent temperature of the hyperfine splitting of the two energy levels [Pritchard and Loeb, 2012].

The globally averaged brightness temperature δT_b depends directly on x_{HI} , z , T_s , and T_{CMB} , but T_s is heavily influenced by T_K and the various coupling mechanisms. x_{HI} is the fraction of neutral hydrogen, the hydrogen spin temperature (T_s) is the excitation temperature of the 21 cm line, kinetic gas temperature, T_K , characterizes the thermal motion of atoms in the gas [Koopmans et al., 2015; Furlanetto et al., 2006]. The equation

$$\delta T_b \propto x_{HI}(1+z)^{1/2}(T_s - T_{CMB})/T_s \quad (1.3)$$

relates δT_b to important factors which are x_{HI} , redshift (z) and two temperatures, the spin temperature (T_s) and the CMB temperature (T_{CMB}).

Figure 1.3 describes the physical processes that are responsible for the frequency structures we see in the evolution of the sky-averaged 21 cm brightness temperature.

1.2.1 Dark Ages

The cosmic dark ages lie between recombination and cosmic dawn, beginning $\sim 380,000$ years after the big bang and ending a few tens of million years later ($1100 > z > 30$) [Jones et al., 2014] during which there were no luminous sources. The cosmic dark ages possess distinctive features that have never been explored to date.

Region A in Figure 1.3 (green) highlights the dark ages period where the free electrons were no longer present. During this epoch, right after recombination, $T_K = T_\gamma = T_s$ where T_γ is the temperature of the radiation background, typically set by the CMB so that $T_\gamma = T_{CMB}$. During this period, matter that had separated

from the CMB was cooled adiabatically as the universe expanded, which led to T_K decreasing below T_γ [Furlanetto et al., 2006]. T_S is initially coupled to T_K as the collision between hydrogen atoms is effective at early times, resulting in δT_b decreasing. As the universe expands and collisional coupling becomes ineffective, T_S reverts to T_γ because of CMB absorption, and δT_b therefore eventually increases.

At this juncture, the most dominating matter in the universe was the dark matter and meager amounts of ordinary matter (neutral hydrogen and helium). After a few hundred million years, the dark and ordinary matter collapse together into halo-like structures through gravitational collapse, steadily cumulating physical matter and finally forming the first stars and galaxies, and that was the end of the cosmic dark ages [Miralda-Escudé, 2003].

1.2.2 Cosmic Dawn

After the first stars' formation, their UV radiation couples to the HI line through the Wouthuysen-Field effect [Pritchard and Loeb, 2012]. Emission of Lyman Alpha photons by the first stars strongly couples T_K and T_S of the IGM; the described period is shown in **Region B** highlighted in purple. The coupling of T_S to T_K leads to a drastic absorption feature in δT_b . The absorption feature can be used to probe the formation processes of the first stars, with the potential of differentiating between Pop II and Pop III stars. **Region C** highlighted in yellow shows a period where the X-rays are emitted by hot accretion disks around the first stellar remnants (e.g., black holes) that effectively heat the cold HI gas. The heating of the neutral gas and constant coupling between T_S and T_K raised the overall spin-temperature to higher than the CMB temperature. Consequently, the 21-cm line became visible in emission at $z \sim 15$. During radiation and heating, these first sources (possibly including mini-quasars) also ionized the gas around them, and a period of reionization started that is thought to have lasted until $z \sim 5$ to ~ 6 [Koopmans et al., 2015]). The detailed δT_b features are sensitive to the black hole properties and the progenitor's metallicity, offering further insight into first-star formation. [Lazio et al., 2016]. **Region D** highlighted in red describes that when reionization begins, the neutral hydrogen supply is depleted (x_{HI} decreases to zero), so δT_b eventually also flatlines to zero because there is no more 21 cm signal left.

1.3 Hydrogen Line Observational Challenges

Redshifted 21-cm radiation can penetrate dust and the Earth's atmosphere and is, therefore, an ideal tool for probing the history of the universe at any epoch of interest. However, ground-based telescopes and experiments are faced with several challenges when it comes to using the redshifted 21 cm line emission to observe the dark ages, cosmic dawn, and the epoch of reionization. The primary challenges are human-made radio frequency interference (RFI), astrophysical foregrounds, ionospheric interference (the ionosphere is nearly opaque below 10 MHz), and instrumental systematics.

Brightness of Foreground Emission

Foreground emission arises from both diffuse Galactic structure and extragalactic sources. The foreground emission's brightness temperatures are 4-5 orders of magnitude brighter than the cosmological 21 cm signal. Galactic synchrotron emission is the primary foreground at low frequency and originates from the Galactic magnetic field's cosmic ray electrons' movement. Free electrons scattering off ions without being captured produces the Galactic free-free emission. The extragalactic foregrounds are predominantly radio-loud galaxies and quasars [Huang et al., 2018; Jelić et al., 2008].

Instrumental Systematics

Global signal experiments measure total power and are therefore dominated entirely by systematics. The 21-cm absorption feature from cosmic dawn has a predicted amplitude of ~ 0.1 mK. To estimate the amount of integration time needed to detect the cosmic dawn feature assuming statistical noise alone, we use the radiometer equation,

$$T_{rms} = \frac{T_{sky}}{\sqrt{B \cdot t_{obs}}}, \quad (1.4)$$

where T_{rms} is the root mean square (rms) fluctuation of the sky temperature, T_{sky} is the sky temperature, B is the observation bandwidth, which can be varied, and t_{obs} is the integration time in seconds. The required observing time can be estimated by

$$t_{obs} = \left(\frac{T_{sky}}{T_{rms}} \right)^2 \times \frac{1}{B}. \quad (1.5)$$

For instance, t_{obs} can be estimated to be 3 h to reach the sensitivity of 100 mK if $T_{rms} \sim 10\text{mK}$, $T_{sky} \sim 1000\text{K}$ and $B = 1\text{MHz}$. This calculation shows that statistical noise is typically not a limiting factor for cosmic dawn experiments.

RFI

Besides astrophysical challenges, human-made RFI saturates many frequency bands, increasing the need for isolated remote deployment sites. RFI can be orders of magnitude brighter than Galactic and extragalactic foregrounds. Unfortunately, RFI introduces a reduction in sensitivity in two separate but distinct ways: direct contamination by having similar spectral characteristics and overpowering the 21 cm signal. The cosmic dawn signal coincides with the FM band (88 MHz to 108 MHz corresponding to $15 > z > 12$), and FM contamination is especially predominant. Like radio transmitters that are run on the ground, satellite or aircraft communications often contribute to RFI. These RFI origins need not be nearby in many instances. Ionized meteor tracks, for example, are known to reflect RFI from remote areas. Inadequately shielded electronics can create self-generated RFI in the telescopes. RFI overpowers the signal from sources of astrophysical origin; therefore, mitigation must be applied. The foremost fundamental procedure for RFI mitigation is to prevent RFI in telescopes by deploying in remote areas. Other than site selection, there needs to be RFI removal during data analysis [Liu and Shaw, 2020].

As much as RFI is challenging to avoid, there are a few restricted circumstances where it can be useful. The Orbcomm satellite transmission around 137 MHz to 138 MHz, for instance, serves as a calibrator source that can be used to provide analytical mappings of an antenna's main beam patterns. With such satellites in low-Earth orbits that precede over time, these sources travel through the field of view of an antenna rapidly and regularly, allowing a relatively densely sampled mapping of the primary beam [Neben et al., 2015; Line et al., 2018].

Ionospheric Contamination

The Earth's ionosphere also introduces significant fluctuations, which becomes increasingly refractive and turbulent below 100 MHz and becomes practically opaque below 10 MHz. In order to minimize RFI and ionospheric contamination, there have been proposals to observe long wavelengths from space-based telescopes further away from the ionosphere of our planet. These space-based telescopes do not exist yet, and there are several ground-based experimental efforts to understand how well we can make measurements from Earth [Chen et al., 2019; Koopmans et al., 2019]. At night near-polar latitudes have lower plasma cutoff frequencies, and the cutoff is reduced during solar minima.

1.4 Previous Cosmic Dawn and Low-frequency Experiments

The 21 cm wavelength of hydrogen gas is being observed by several experiments designed for Hydrogen mapping in our universe. Despite the challenges that are encountered in 21 cm cosmology, many experiments are nevertheless underway. This section highlights experiments aimed at frequencies corresponding to the dark ages ($1100 \lesssim z \lesssim 30$) and cosmic dawn ($30 \lesssim z \lesssim 10$).

1.4.1 Global Signal Experiments for Cosmic Dawn

The global signal experiments are most commonly located in remote RFI-quiet areas using single antennas with a large solid angle observing total power. However, there have been suggested and attempted innovative methods using interferometry.

The Experiment to Detect the Global EoR Signature (EDGES) is located at Murchison Radio-astronomy Observatory (MRO) in Western Australia. The project's goal is radio detection of characteristic hydrogen signatures from cosmic dawn and the epoch of reionization. EDGES consists of a high-band instrument operating over the 90-200 MHz ($14 > z > 6$) range, a mid-band instrument operating over 60–160 MHz, and a low-band instrument that is sensitive to the 50-100 MHz ($27 > z > 13$) range [Monsalve et al., 2017].

The first detection of the 21 cm global signal was reported by Bowman et al. [2018] as a flattened absorption profile centered at a 78.1 MHz frequency, with an amplitude of 0.53 K and width of 18.7 MHz. The amplitude is more than a factor of two larger than the most optimistic model where no heating occurs until $z \sim 17$, thus suggesting a hotter background or a colder than expected primordial

	Site	Frequency	Instrumental Approach
CTP	Troy, Virginia	60–120 MHz	Dual-polarization Dipole
EDGES	Western Australia	50–200 MHz	Single-polarization Dipole
LEDA	Owens Valley	10–88 MHz	251 Dual-polarization Dipoles
MIST	MARS	5–200 MHz	One Dipole Antenna
PRI ^Z M	Marion Island	30–200 MHz	2 Dual-polarization Dipoles
REACH	South African Karoo desert	50–200 MHz	Monopole Antenna
SARAS2	Gauribidanur Obs., India	87.5–175 MHz	Fat-dipole Antenna

Table 1.1: Active and upcoming global signal experiments. CTP, EDGES, LEDA, MIST, PRI^ZM REACH and SARAS 2 experiments with their deployment sites, frequency ranges and instrumental approach. EDGES experiment is discussed in detail on text.

gas. The detection has spurred multiple interpretations of new physics, including collisional dark matter [Barkana, 2018; Barkana et al., 2018]. Independent verification by similar experiments is therefore of utmost importance.

Other global signal experiments are summarised in Table 1.1. The included experiments are the Cosmic Twilight Polarimeter (CTP, Nhan et al. [2019]), Large aperture Experiment to Detect the Dark Ages (LEDA, Taylor et al. [2012]; Price et al. [2018]), Mapper of the IGM Spin Temperature (MIST, Monsalve et al.), PRI^ZM, Philip et al. [2019], Radio Experiment for the Analysis of Cosmic Hydrogen (REACH, de Lera Acedo [2019]), and the Shaped Antenna measurement of background RAdio Spectrum 2 (SARAS2, Patra et al. [2013])

1.4.2 Imaging below 30 MHz

Long Wavelength Astronomy Background

The father of radio astronomy, Karl G. Jansky, played a massive role in the inauguration of radio astronomy dating back to 1931. At that time, he was an employee at the Bell Telephone Laboratories as a radio engineer. Jansky was allocated to study and solve the problem that hindered the radio communication systems. Using highly directive antenna arrays shown in Figure 1.4, he discovered that the static caused the radio frequency noise that hindered the communication systems from thunderstorms [Fisher Miller, 1998; Kraus, 1986].

The antenna that he constructed operated at an approximated frequency of 20 MHz, corresponding to an approximate long wavelength of 15 m. He further found radio radiation from the Galactic Center at the operating frequency. Out of interest in Jansky’s instigating discoveries, Grote Reber designed a radio telescope that operated at a range of approximately 10 MHz to 160 MHz (30 m-2 m wavelength) in 1937. He discovered that the dominant source at longer wavelengths was the Milky Way. Furthermore, he realized that the radio telescope acts like a bolometer or a device to measure the heat. The antenna’s radiation resistance measures an equivalent temperature of a distant part of space to which the 24 antenna response pattern projects it [Reber, 1988, 1942; Hicks et al., 2012].

Because of the research done for the communication systems, radio astronomy was born and expanded to radio astronomy and astrophysics [Hicks et al., 2012]. The hydrogen line research area had an accelerated discovery, which was

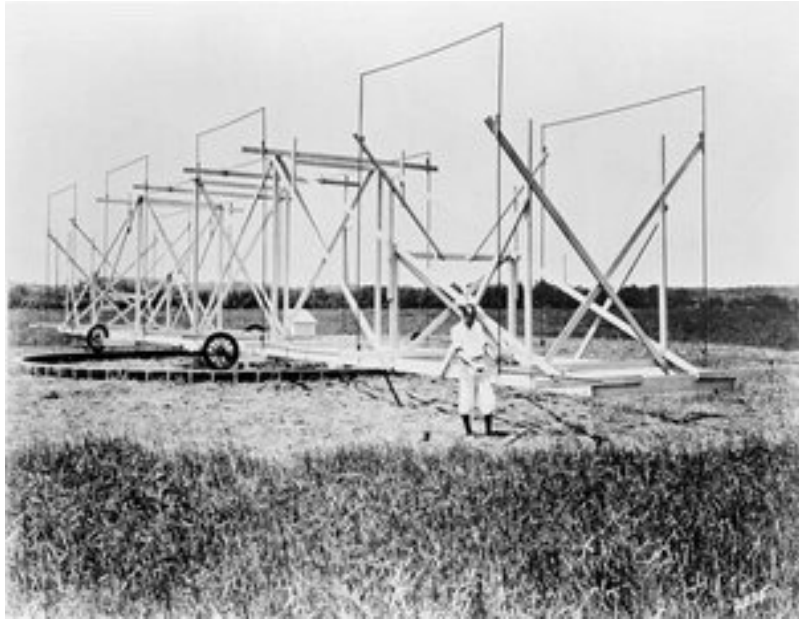


Figure 1.4: Jansky's highly directive antenna arrays which he used to discover the cause of RFI that hindered the communication systems at Bell Telephone Laboratories [Fisher Miller, 1998]

allocated an operating frequency of 1420 MHz (21 cm wavelength) [Lovell, 1961]. After all these discoveries, the long-wavelength astronomy fascination has been resuscitated in the present epoch.

Long Wavelength Astronomy Experiments

There are quite a few low-frequency experiments, but this document will briefly discuss a few measurements that exist at $\lesssim 30$ MHz. Two of these experiments represent the lowest frequencies measured to date (Reber's antenna, RAE-B). The other two represent the highest resolutions achieved in this frequency range (DRAO, OVRO-LWA).

Grote Reber constructed a state-of-the-art telescope operating at very low frequencies between 0.52 MHz and 2.1 MHz, which had 192 dipoles. At 2.1 MHz, the array had a resolution $\sim 5^\circ$ and was able to map the sky. The measurements were dominated by Galactic emission and the ionosphere as shown in Figure 1.5 [Reber, 1988].

The Radio Astronomy Explorer-2 (RAE-2) operated between 25 kHz and 13 MHz, with the primary science goal of radio measurements of our Galaxy, the Sun, Earth, and all the other planets. The resolution of this experiment is $\sim 10^\circ$ at 4.7 MHz [Alexander et al., 1975].

Higher-resolution experiments include the OVRO-LWA, Dominion Radio Astrophysical Observatory (DRAO) 22 MHz telescope, and the DRAO 10 MHz array. The OVRO-LWA operates at frequency ranges of 36.528 MHz and 73.152 MHz. At these frequencies, it has an angular resolution of $15'$ [Eastwood et al., 2018]. The DRAO telescope operated at 22 MHz, and its resolution ranges between $\sim 1.1^\circ$ - 1.7° . Its primary science goal was to measure the emission from discrete sources and observe our Galaxy's emission from its environment [Roger et al., 1999]. The

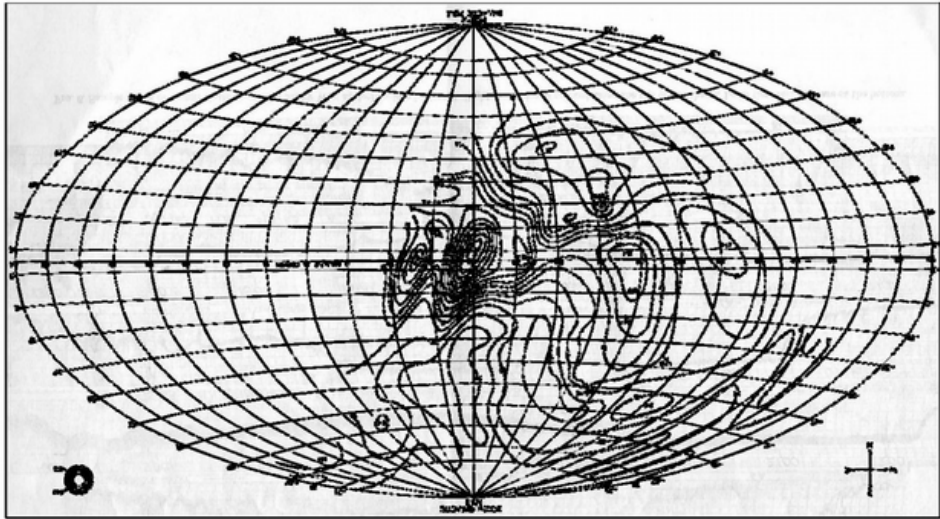


Figure 11: A 2.085 MHz contour map of galactic radio emission (after Reber, 1968: 10).

Figure 1.5: Grote Reber's state-of-the-art map. The constructed array operated at very low frequencies between 0.52 MHz and 2.1 MHz and at 2.1 MHz, the array had a resolution of $\sim 5^\circ$. It was able to map the sky, and the measurements were dominated by Galactic emission and the ionosphere [Reber, 1988].

DRAO 10 MHz array operated had a resolution of $\sim 2^\circ$, and it was first used for discrete sources and was later used to map the large-scale structure of the background radiation [Caswell, 1976].

1.5 Structure of this Thesis

The focus of my thesis is ALBATROS, which is a new experimental effort aimed at mapping the low-frequency sky with the ultimate objective of mapping the dark ages, and the PRI^ZM experiment which is intended to search for the feature of cosmic dawn absorption in globally averaged redshifted 21-cm emission. The following is the outline of this thesis: in Chapter 2, Marion Island is introduced, the observing location of PRI^ZM and ALBATROS. A summary of my voyage to Marion will also be provided. Chapter 3 will provide a full description of the ALBATROS instrument. Chapter 4 will provide a brief description of the PRI^ZM instrument and present a summary of various system stages. In Chapter 5, preliminary results will be presented and conclude in the same chapter. My main contributions are listed below:

- Designing a prototype solar power supply system in preparation for the 2019 Marion voyage,
- Site inspection and installation of the first ALBATROS autonomous station at Marion Island in 2019,
- Helping with the revision and new designs of the PRI^ZM subsystems, including the front end electronics enclosure, switch control circuit,
- Designing the PRI^ZM second stage electronics enclosure, which was in preparation for the 2020 deployment that did not happen.

Chapter 2

Observing at the Marion Island Site

Observing at the Marion Island site comes with consequences that need to be addressed. Those factors mainly affect the low-frequency experiments (PRI^ZM/ALBATROS) discussed in this thesis, and they include RF quietness, ionospheric conditions, accessibility, and ability to support long baselines. Low-frequency observations require high angular resolution to improve the experiment's sensitivity. Systematics discussed in §1.3 widely dominate the experiments operating at frequencies <200 MHz. RFI from the frequency modulation (FM) transmitters is a substantial contributor in the low-frequency regime; thus, FM contamination is widespread into observation bands. Observing from remote deployment sites is a solution to the FM band contamination issue. Before site selection and deployment, radio environments must match the specific instrument's requirements when assessed. Accessibility is a common challenge that arises from remote site selection. Therefore, choosing a good observing location is generally a balance between accessibility and radio-quietness.

Marion Island was chosen as the observing site for PRI^ZM and ALBATROS after evaluating the mentioned factors. Marion Island is the exceptionally radio-quiet environment for low-frequency observations, although the site is only accessible annually. The next section discusses the location in more detail.

2.1 Marion Island

Marion Island is a research base that forms part of the Prince Edward Islands shown in Figure 2.1, located in the southern Indian Ocean at 46°54'45"S, 37°44'37"E. The South African National Antarctic Programme (SANAP) and the South African Department of Environmental Affairs (DEA) operate the research base shown in Figure 2.2. The island is ~ 2000 km from the nearest continental landmasses, has an area of 290 km², and the main base is positioned on the northeast side. Marion Island has a volcanic origin, and the terrain is scattered with many secondary craters and small lakes. There are abundant snow and rain, and the vegetation is mainly mosses and ferns. The lowland regions are marshy due to high precipitation. It is incredibly windy and mostly cloudy throughout the year.

The DEA owns the S. A. Agulhas II ¹, a South African ice-breaking polar supply and research ship that services the island every year in April. During the relief

¹https://en.wikipedia.org/wiki/S.A._Agulhas_II

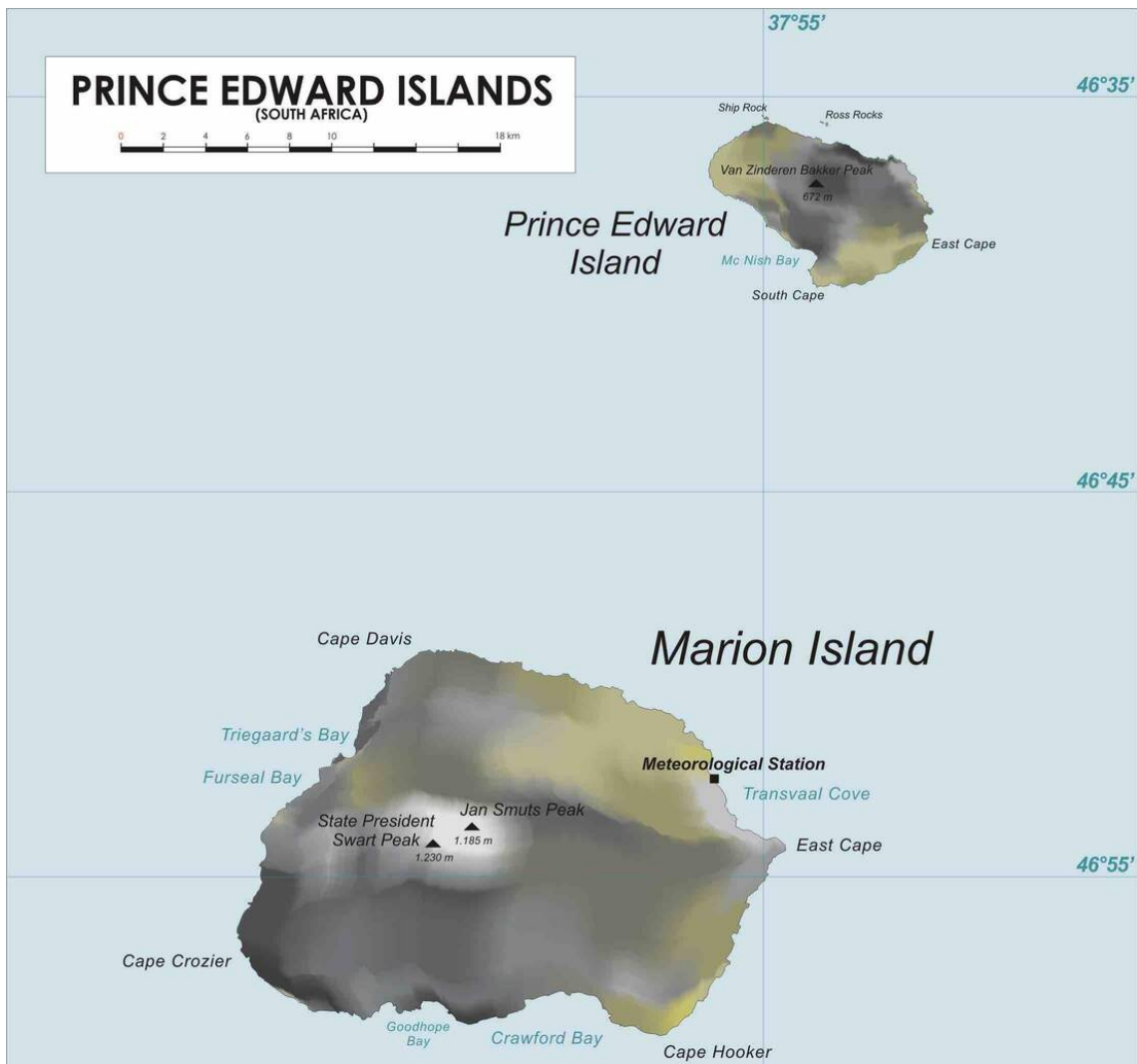


Figure 2.1: The two islands in the Prince Edward Islands are Prince Edward Island and Marion Island, located in the sub-Antarctic Indian ocean [PEI, 2007]



Figure 2.2: Marion Island new (yellow buildings) and old base (white buildings). The green building partially visible behind the new base is the emergency base that serves as a helipad and a hangar for helicopter operations.

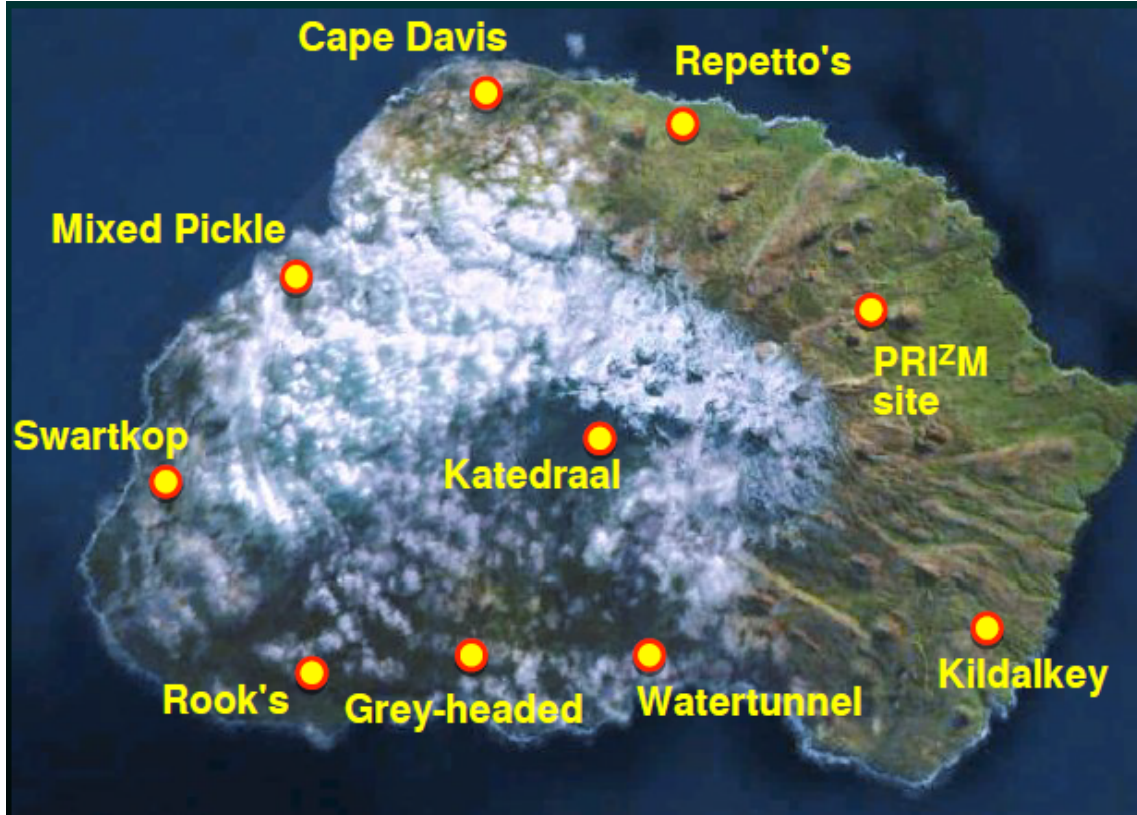


Figure 2.3: Marion Island rest huts and the PRI^ZM site where the first radio astronomy instrument was deployed and subsequently ALBATROS pathfinder.

voyage in April, three weeks are spent on the island deploying and maintaining instruments. Marion Island has been traditionally used for the research fields of space weather, geology, meteorology, mammalogy, ornithology, and botany. The main Marion base accommodates all the researchers participating in the relief voyage and overwintering team members. Figure 2.3 shows the nine rest huts (Kildalkey, Watertunnel, Cape Davis, Grey-headed, Mixed Pickle, Repetto's, Rooks, Swartkops, and, Katedraal) that researchers use while traversing the island. The PRI^ZM instrument was deployed 4 km southwest of the main base ($46^{\circ}53'13''S$, $37^{\circ}49'10.7''E$) as the first radio astronomy experiment in Marion Island, followed by the ALBATROS pathfinder instruments on the same site.

2.2 Advantages of Observing from Marion Island

This section presents a brief overview of the site selection process on Marion, and a full description is available in Philip et al. [2019]. In choosing the observing site for PRI^ZM and ALBATROS, several radio spectrum measurements were done on different sites, including the South African Karoo desert. The radio-quiet environment of Marion Island surpasses that of the South African Karoo desert, as shown in Figure 2.4. At Marion Island, there is no evident detection of RFI contamination in the FM band, and the only significant RFI visible within the PRIZM operating range is Orbcomm satellite transmission at 137 MHz to 138 MHz and the 250 MHz FPGA clock artifact visible at 125 MHz. The enhanced RFI from meteor

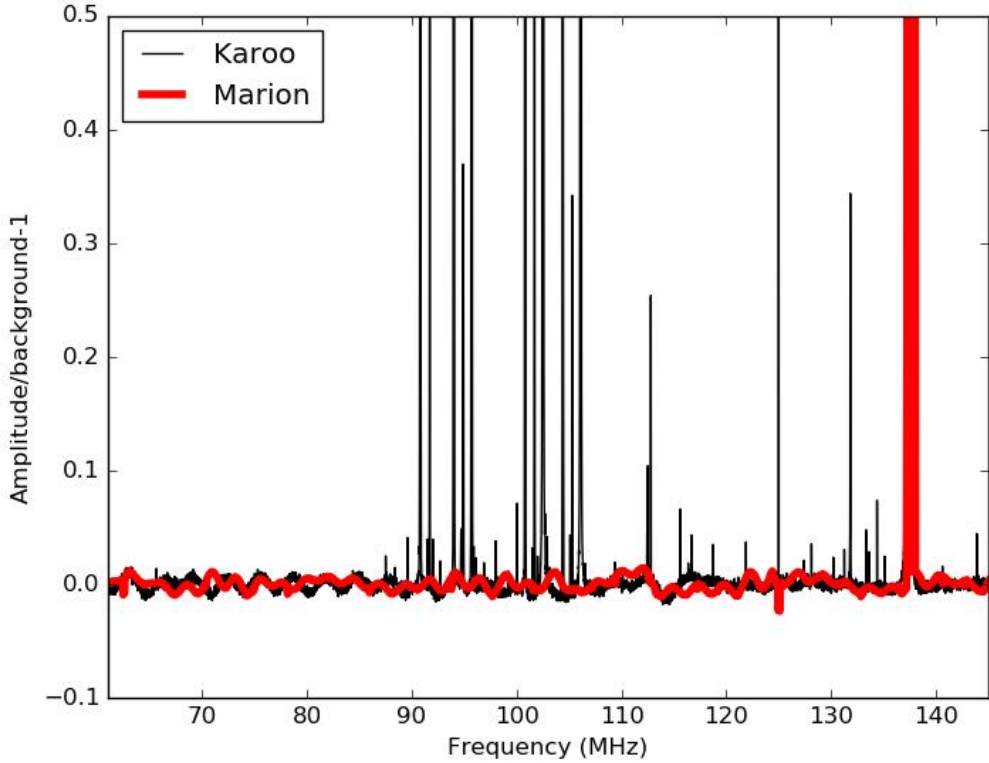


Figure 2.4: Radio spectrum contrast on Marion (thick red) and in the Karoo Desert (thin black). Without RFI excision, the fractional amplitude above the background matches the raw and uncalibrated data. At 137-138 MHz, the Orbcomm satellite transmission is visible; Marion’s data has no visible RFI. The 125 MHz feature is an artifact of the 250 MHz FPGA clock and not because of RFI. [Philip et al., 2019]

scattering is a common phenomenon in several remote sites excluding Marion Island, as there have not been evident measurements of such RFI. At a speed of $\sim 10 \text{ km s}^{-1}$ to 75 km s^{-1} , meteoroids enter the Earth’s atmosphere, and contact with the atmosphere results in the air molecules ionization. During this time, by bouncing radio waves off the ionized trail, brief contact paths can be formed between radio stations several thousand miles away from each other. Likewise, terrestrial RFI sometimes gets scattered off the trail over long distances. Depending on the meteor trail’s location and the intensity of meteor activity, RFI’s magnitude due to meteor dispersion varies [Wislez, 1996].

Figure 2.5 shows the RFI spectrum comparison between the PRI^ZM deployment site 4 km away from the island’s main base. The selection of PRI^ZM site was based on having a reasonably dry and even terrain, i.e., not in a mire, a reasonable hiking distance from the main base, and keeping the locally generated RFI at its minimum. Locally generated RFI is reduced at the PRI^ZM site, since Junior’s Kop is situated between the deployment site and the island’s main base, providing enhanced RFI shielding of $\sim 60 \text{ dB}$. The reduction in power arises from a physical distance from the base and the landmass in Junior’s kop. A helicopter was operating near the base when the RFI measurements were taken and was

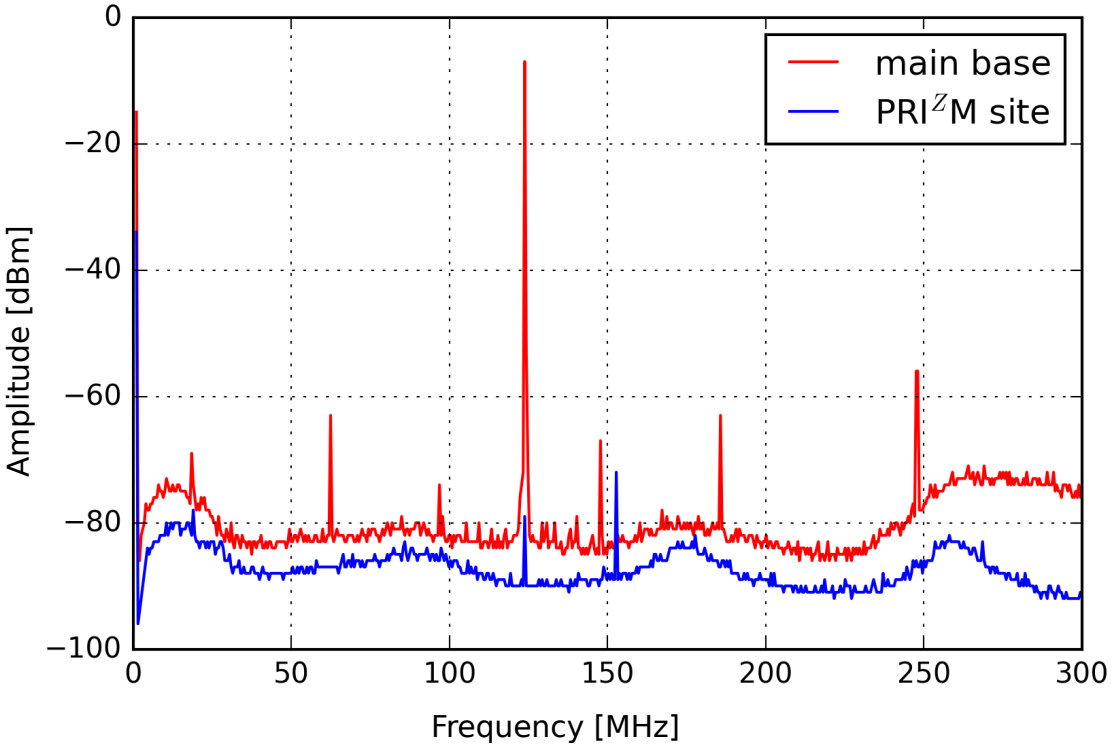


Figure 2.5: RFI measurement differentiated from the Marion base and the PRI^ZM observing site. When the measurements were taken, the spectrum analyzer was set to max hold, and the measurement period coincided with the helicopter’s operation near the base and transmitting at 123.45 MHz. A rough benchmark of \sim 60 dB signal suppression in received power at both locations arising from a combination of attenuation from Junior’s kop and the distance between the PRI^ZM site and the base. The peak at 156 MHz is a transmission from a handheld radio [Philip et al., 2019].

transmitting at a frequency of 123.45 MHz. The helicopter’s transmission line was an unexpected RFI origin that enabled the rough calibration of the relative levels at Junior’s kop vs. the main base.

Figure 2.6 shows the international reference ionosphere (IRI) model [Bilitza, 2018] predictions illustrating the minimum ionospheric plasma cutoff frequency during the last solar minima. The development of new low-frequency experiments is predominantly driven by the lack of knowledge of what lies in the sky at frequencies \lesssim 30 MHz. According to the IRI model prediction, measurements of the sky at \lesssim 30 MHz do not look entirely impossible because, during the last solar minimum, the ionospheric plasma cutoff frequency was predicted to be \sim 1.5 MHz at Marion Island. Since another solar minimum is being experienced [Bhowmik and Nandy, 2018], it is an excellent opportunity to develop and implement new low-frequency observations. The prediction shows Marion Island, Dome C in Antarctica, and Hobart in Tasmania, where Reber performed his 2 MHz observation. They have the potential to provide new views of the Earth’s ionosphere, which absorbs and refracts at radio frequencies and becomes utterly opaque below the plasma cutoff frequency.

The total Marion takeover voyage period is \sim one and a half months. This pe-

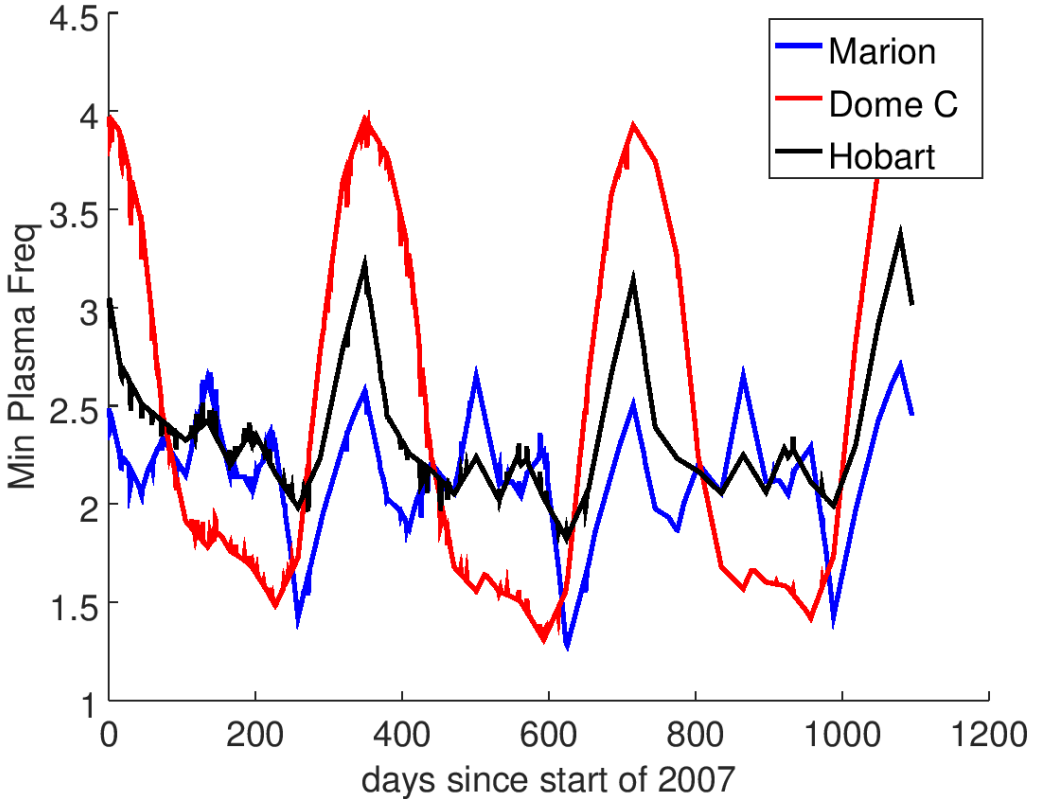


Figure 2.6: The International Reference Ionosphere model predictions illustrating the minimum ionospheric plasma cutoff frequency during last solar minima. At Marion Island, Dome C in Antarctica and Hobart in Tasmania the plasma frequency may drop as low as ~ 1.5 MHz [Chiang et al., 2020].

riod is further shortened by the days it takes to and from the island, the weather, and logistical delays. The site is entirely inaccessible on days with gale-force winds (roaring forties)—the sun sets early, limiting the daylight and more extended access to the instruments. The site’s path is riddled with lava rocks and secret mires, rendering the trek incredibly difficult. Furthermore, the island is an environmentally protected area that sets the boundaries on equipment installations. Although it is a pretty steep price to pay, the reward is an exceptional RF-quiet environment. In the next two chapters, the PRI^ZM and ALBATROS experiments are discussed in detail.

Chapter 3

ALBATROS Experiment

ALBATROS will be an interferometric array consisting of ten autonomous antenna stations operating at a frequency range of 1.2 MHz to 125 MHz that will map the low-frequency sky and will be separated by maximum baseline lengths of ~ 20 km. This experiment is exploratory and will be taking steps towards achieving the future objective of imaging the sky at frequencies that have been unexplored since the 1970s. These observations may allow us to probe even earlier epochs of the universe's history and will lay the groundwork for eventually exploring the cosmic "dark ages."

In April 2019, I was part of the deployment team in Marion Island, and I am going to discuss in detail the tasks associated with ALBATROS that we managed to complete during the three-week relief voyage.

3.1 Overview of the Pathfinder

The ALBATROS pathfinder shown in Figure 3.1 was introduced as an explorer in April 2018 at the PRI^ZM site located approximately 4 km from the main base. The main goal of the pathfinder was to assess the observable frequencies from Marion below 30 MHz. The pathfinder uses two off-the-shelf dual-polarization LWA dipole antennas, configured as a two-element interferometer using direct correlation. The antennas are separated on the east-west baseline and are connected via a 100 m long coaxial cable to the shipping containers that house the readout electronics and serves as the command module. Figure 3.2 shows the block diagram of the pathfinder, and the signal chain description is below.

3.2 Pathfinder System Signal Chain

3.2.1 Antenna

The pathfinder uses two Long Wavelength Array (LWA) antennas configured as a two-element interferometric array. The two dual-polarization antennas are separated by ~ 110 m on an east-west baseline. The LWA antennas were selected for this project because they are relatively simple and are omnidirectionally patterned. The other important factor is that the LWA antennas have a long development history and therefore are a natural off-the-shelf choice for initial measure-

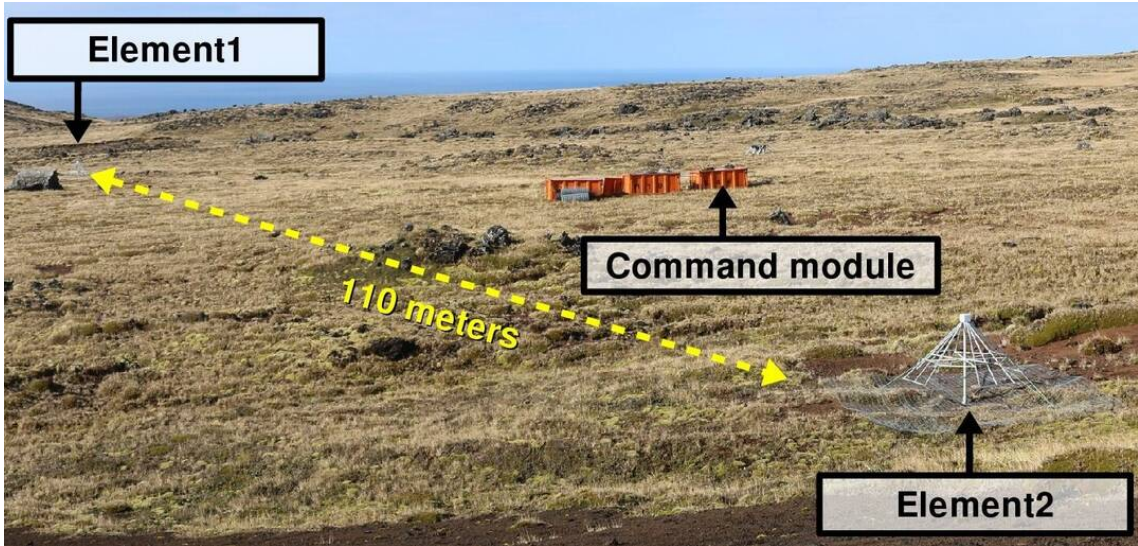


Figure 3.1: The two-element, directly correlated ALBATROS pathfinder installed at the PRI²M site. The pathfinder comprises two dual-polarization antennas separated by roughly 110 m on an east-west baseline. Coaxial cables connect the antennas to an orange shipping container that houses the readout electronics and serves as the "command module".

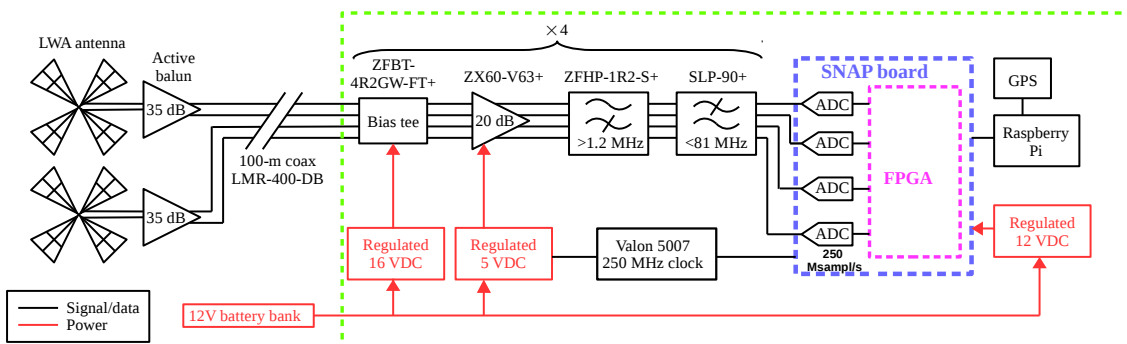


Figure 3.2: The pathfinder's two-element ALBATROS block diagram. The signals from two dual-polarization LWA antennas [Hicks et al., 2012] are amplified by front-end active baluns. The 100-m coaxial cables connect the SSE housed in a Faraday cage denoted by a green dashed box, with the antennas. A second-stage electronics chain is moved to each of the four antenna outputs. It consists of filters and further amplification. A SNAP module comprises an on-board FPGA that calculates auto- and cross-spectra at 250 Msamp/s from and between the four inputs and digitizes the signals. A SNAP board is controlled by the Raspberry Pi, and the data is saved.

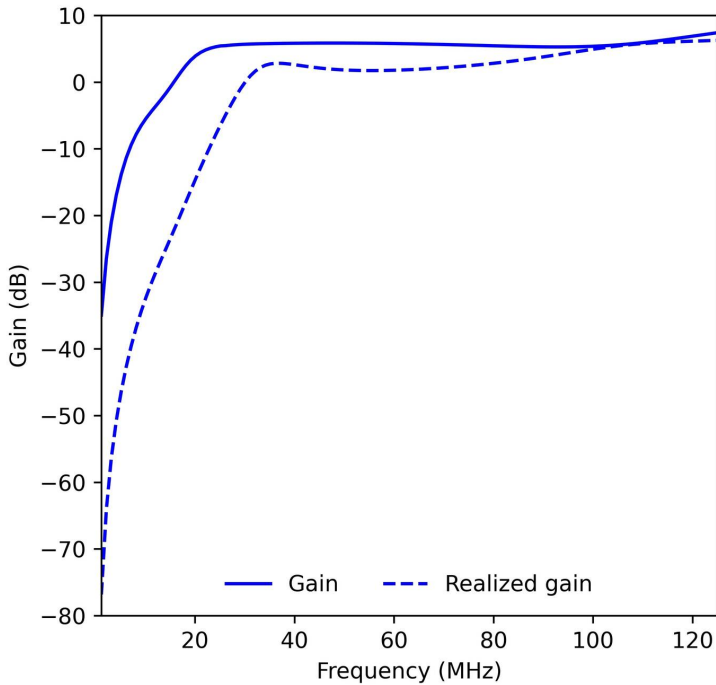


Figure 3.3: FEKO simulation for the antenna gain. The plot shows the gain in the zenith direction (which is always the peak gain) as a function of frequency; it also gives the realized gain (same direction), showing how the antenna is quite lossy. Due to the antenna being electrically short at the lowest frequencies, impedance mismatch losses are high. As a result, the realized gain curve is 50 dB lower. Image credit: Tristan Mérnard

ments. The antennas possess low gain; therefore, the Galactic noise is limited by a factor of 10 at a frequency range of 30 MHz to 90 MHz [Ellingson and Kramer, 2004; Ellingson, 2005]. Figure 3.3 shows the gain in the zenith direction as a function of frequency. It also gives the realized gain (same direction), showing how the antenna is quite lossy at the lowest frequencies. Realized gain also takes into account the losses on the antenna. Due to the antenna being electrically short at the lowest frequencies, impedance mismatch losses are high. As a result, the realized gain curve is 50 dB lower. The dB scale emphasizes how low gain/low efficiency the antenna is outside of its nominal operating range. The entire antenna and supporting structure sits on top of a ground screen that is roughly 3 m on a side and is made of welded wire mesh. To prevent loss by absorption into the ground and also to stabilize the system temperature by isolating the antenna from a variable (e.g., dry versus wet) ground conditions, a conducting 3 m on a side ground screen is necessary [Ellingson et al., 2009].

3.2.2 Front-end Electronics

All the front end electronic (FEE) components are incorporated into a double-sided printed circuit board (PCB) as shown in Figure 3.4a and the block diagram

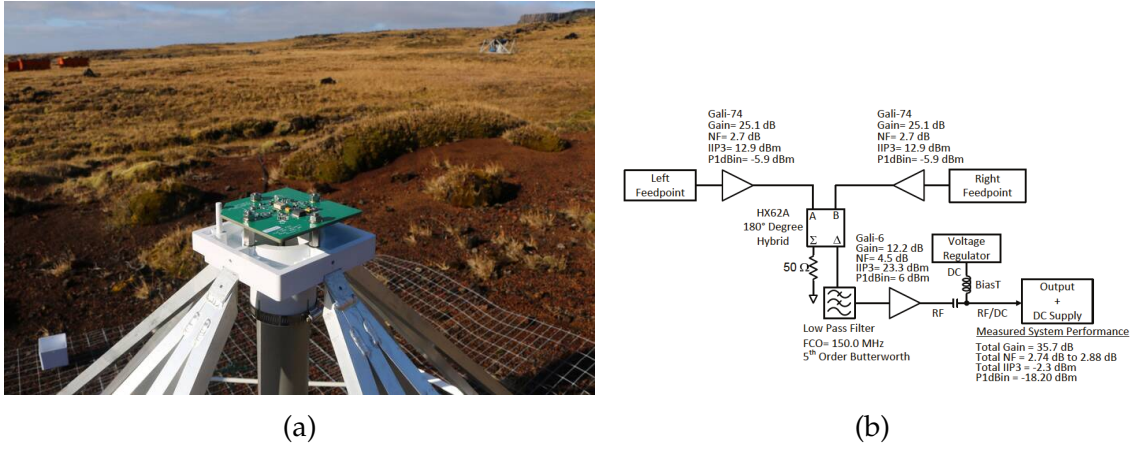


Figure 3.4: (a) Unenclosed FEE mounted on the pathfinder antenna supporting structure with the electronic components visible on the top part of the PCB. (b) One polarisation block diagram of the FEE [Hicks et al., 2012]

is shown in Figure 3.4b. One side of the PCB is a solid copper ground plane, and the other side is populated with components. The solid copper ground plane is aperiodically stitched to the grounded copper on the side populated with components. The active balun provides an input impedance of $50\ \Omega$ to each dipole. The Mini-Circuits GALI-74+ monolithic microwave integrated circuit (MMIC) amplifiers from both feed points amplify each signal by +24 dB of gain. A passive 180° hybrid coupler differentiates the two GALI-74+ outputs. A low-pass filters the coupler output by 150 MHz and gains 12 dB from the Mini-Circuits GALI-6+ MMIC. The signal gets fed to a second amplifier. The output impedance of the FEE is matched to a $50\ \Omega$ 100 m LMR400 coaxial cable having a nominal attenuation of $\sim 0.4\text{ dB}/100\text{ m}$ to $3.7\text{ dB}/100\text{ m}$ at 1.2 MHz to 81 MHz. The Mini-Circuits ZFBT-4R2GW-FT+ bias tee powers the FEE by 16 V and extracts the RF signal by the use of the coaxial cable. The FEE has an overall gain of ~ 36 dB and an overall noise figure of ~ 2.7 dB to ~ 2.9 dB [Hicks et al., 2012; Ray et al., 2006].

3.2.3 Back-end Electronics

The back-end electronics are housed in the Faraday cage shown in Figure 3.5a and denoted by the green dotted line box in Figure 3.2. The analog signal chain consists of a Mini-Circuits ZX60-V63+ amplifier with a 20 dB gain, and a set of high- and low-pass filters (Mini-Circuits ZFHP-1R2+ and SLP-90+) that together band-limits the signal to 1.2 MHz to 81 MHz. The amplifier operates at a frequency range of 50 MHz - 6 GHz and has a noise figure of ~ 3.6 dB at its lowest operating frequency of ~ 50 MHz. The high- and low-pass filters present a nominal insertion loss of 0.2 dB and 0.14 dB at the center frequency of ~ 10 MHz, respectively. AWR design environment simulation and analysis were used as shown in Figure 3.6 to plot the combined transfer function of the analog chain. The plot combines the S21 magnitudes in dB of the low pass filter, high pass filter, and amplifier. It clearly shows that the cutoff frequency is ~ 90 MHz corresponding to the ~ 20 dB magnitude in dB.

A Smart Network ADC Processor [SNAP; Hickish et al., 2016] mounted in the Faraday cage in Figure 3.5b samples incoming signals at 250 Msamp/s using



Figure 3.5: **(a)** The Faraday cage housing the ALBATROS back-end electronics. The box mounts all components back-to-back on a central shelf so that everything can be accessed by opening opposing sides. One side of the mounting plate shows the amplifiers, pair of high- and low-pass filters, bias-tees, Valon 5007 frequency synthesizer module, RPi and Adafruit Ultimate GPS module. Component not visible on this side are mounted on the other side of the mounting plate. **(b)** The bottom side of the ALBATROS Faraday cage, showing the mounted SNAP board and the regulatory circuit.

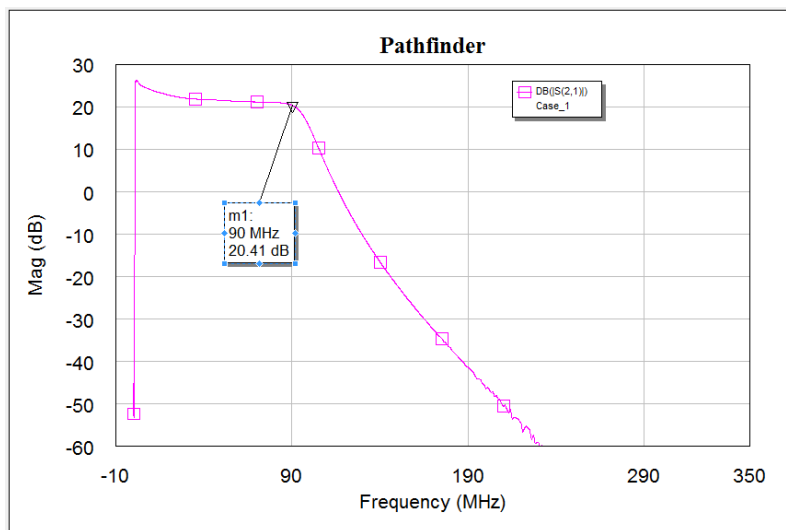


Figure 3.6: A combined transfer function of the analog chain. The plot is a combination of the S21 magnitudes in dB of the low pass filter, high pass filter and the amplifier. The cutoff frequency is at ~ 90 MHz.

Module	Power Dissipation (W)	Voltage (V)	Current (A)
SNAP board	~30	12	2.5
FEE and Dual Pol	~8	16	0.48
2nd Stage Amplifier	~0.7	5	0.14
5007 Frequency Synthesizer	~2	5	0.4
RPi	~12.5	5	2.5
Total	~53.2		~6

Table 3.1: The two-element pathfinder system ratings. The figures shown are from the datasheets of the various components and considering that the antennas are dual-polarization antennas.

internal analog to digital converters (ADCs), with a clock signal provided by a Valon 5007 frequency synthesizer module. A frequency range between 0 MHz to 125 MHz containing 2048 channels is created by the SNAP board, which also includes the on-board Xilinx Kintex 7¹. The FPGA is programmed with spectrometer firmware that channelizes the ADC data and computes auto- and cross-spectra. The SNAP board is controlled by a Raspberry Pi (RPi), and the data rate of the average spectrum is about 400 MB/day (with compression), and this low volume allows the spectra to be stored on the RPi on-board SD card. The RPi absolute timing is provided by Adafruit Ultimate GPS module², connected to an active external GPS antenna.

3.2.4 Power

The two-element pathfinder system is powered using four 12 V, 200 A h batteries wired in parallel, and charging is performed manually using a Honda EU30is³ generator and a fuel cache that is kept at the observing site. The main advantage of using a SNAP board is its low power consumption, which enables long-term battery-powered operation. The total system power draw is ~45 W and the pathfinder system can operate without interruption for ~1 week when the batteries are fully charged. Table 3.1 shows a rough power budget of the pathfinder system, taking into consideration the dual polarization antennas. During observations, the batteries are connected to DC/DC converters powering the SNAP board, FEE, amplifiers, and the clock. The DC-DC converters are housed inside the Faraday cage and provide 12 V stable voltage output distributed to the buck and boost converters. An output of 16 V from the boost converter powers the FEEs via the coaxial cable using the bias tees, the SNAP board is powered directly from the DC-DC converters, the amplifiers are powered by 5 V from the buck converter.

¹<http://www.xilinx.com/products/silicon-devices/fpga/kintex-7.html>

²<https://www.adafruit.com/product/746>

³<http://www.hondaenergy.com/generators/honda-eu30is.html>

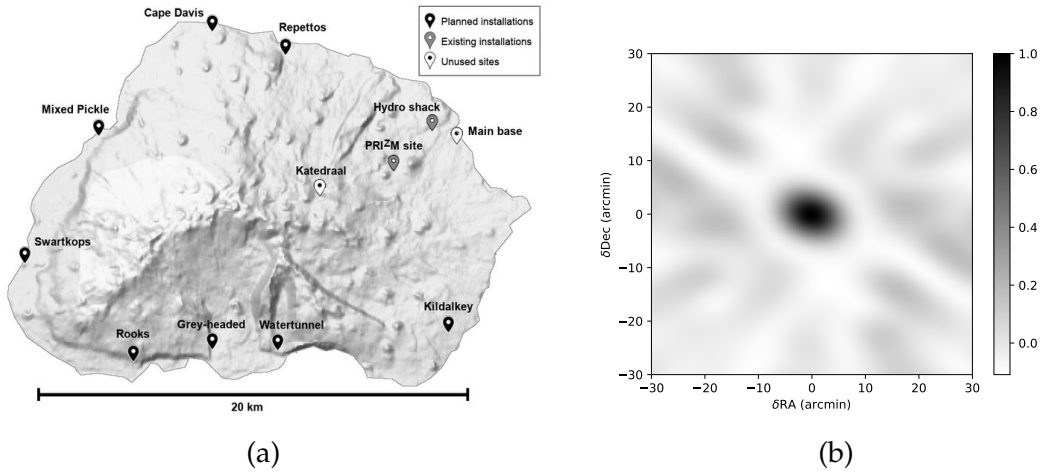


Figure 3.7: (a) Marion Island map. The ALBATROS pathfinder antennas are presently located at the PRI^ZM site and the hydro shack (gray markers). The ones marked in black indicate the eight shore huts that will be used for potential installations of the ALBATROS antennas. The white markers show the other infrastructure points available that will not be used for antennas. (b) 5 MHz synthesized beam at zenith from the complete ALBATROS array, using the current and scheduled installation locations shown on the map. A synthesized beam is obtained using an octave of bandwidth spanning 3.5–7 MHz in a single snapshot with a FWHM of $\sim 7'$.

3.3 Overview of Autonomous Stations

The final ALBATROS array will consist of ten autonomous antenna stations separated by maximum baseline lengths of ~ 20 km as shown in Figure 3.7a. There are eight remaining planned installation sites. The Hydro shack and the PRI^ZM site already have infrastructure installed, and Katedraal will remain unused. The ten installation sites (existing and planned) for the ALBATROS array have a ring-like pattern that is appropriate for imaging and produces an FWHM synthesized beam of $7'$ at 5 MHz as shown in Figure 3.7b. The array beam promises an improved (> 10 times better) resolution over existing measurements to date. Thus far, the ALBATROS main goal will be to map Galactic foregrounds at high resolution at low frequencies, which is crucial before doing cosmological observations of the dark ages.

In April 2019, I was part of the deployment team in Marion Island, and I am going to discuss in detail the tasks associated with ALBATROS that we managed to complete during the three-week relief voyage.

3.4 2019 Marion Voyage

The S. A. Agulhas II sails from Cape Town each year in April. The relief voyage preparations begin months before the ship sails; the team plans and makes decisions based on the next voyage's goals. One of the primary goals of the 2019 voyage was to install the prototype autonomous station. The goal was to conduct an end-to-end system test under Marion's environmental conditions. The

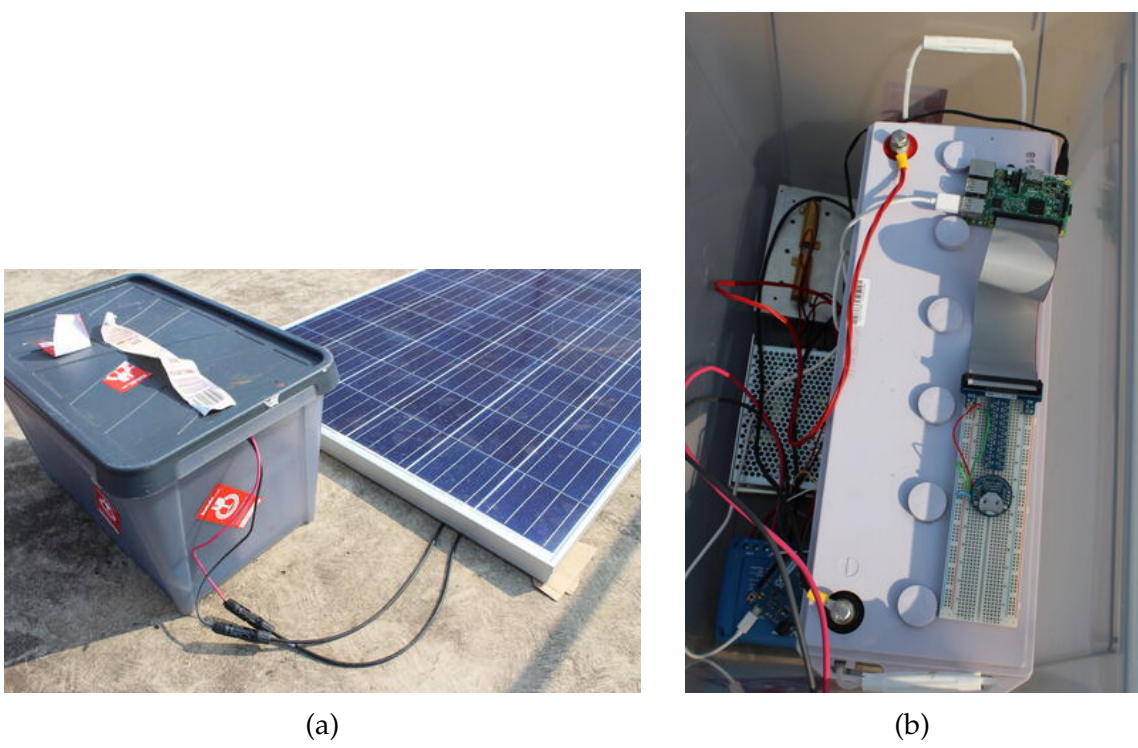


Figure 3.8: **(a)** A prototype solar power supply setup. The prototype of the proposed system was tested on the roof of H Block at the UKZN. The solar panel which was used was the Enersol 300 and the control electronics are enclosed in the weather proof plastic bin. **(b)** Interior of the enclosure. Inside the enclosure was the solar regulator which was monitored via a communication port, a single 12 V 150 A h battery, an Arduino board which was programmed for serial to Universal Serial Bus (USB) communication, the Rpi which was connected to the sdr clock module for proper timing and synchronization stored the data which was monitored from the solar regulator, the DC-DC converter regulated the voltage to the $6\ \Omega$ high power resistor.

solar power budget, mechanical/electrical survival in wind and rain, and mouse proofing was the most critical considerations that were evaluated. The development and testing of improved designs and systems occur at the University of KwaZulu Natal radio astronomy lab.

In preparation for the 2019 voyage, I designed and developed a prototype solar power supply system that paved the way for the solar power supply system installed in Marion Island as part of the autonomous stations. Figure 3.8a shows the solar panel used and the bin that enclosed the control electronics for the solar power system. Figure 3.8b shows the solar charge controller (Victron BlueSolar MPPT 75|15), 12 V 150 A h battery, an Arduino that was used for logging the data from the solar charge controller to an SD card mounted in the RPi.

Because of the weather conditions in Marion Island, the pathfinder system can shut down for an extended period without observations. A solar power supply system was selected because the ALBATROS stations are required to run continuously without manual intervention and charging. Therefore, the solar panels need to be appropriately sized, given the power budget and frequently overcast conditions. Also, interferometers are less susceptible to RFI that might be locally

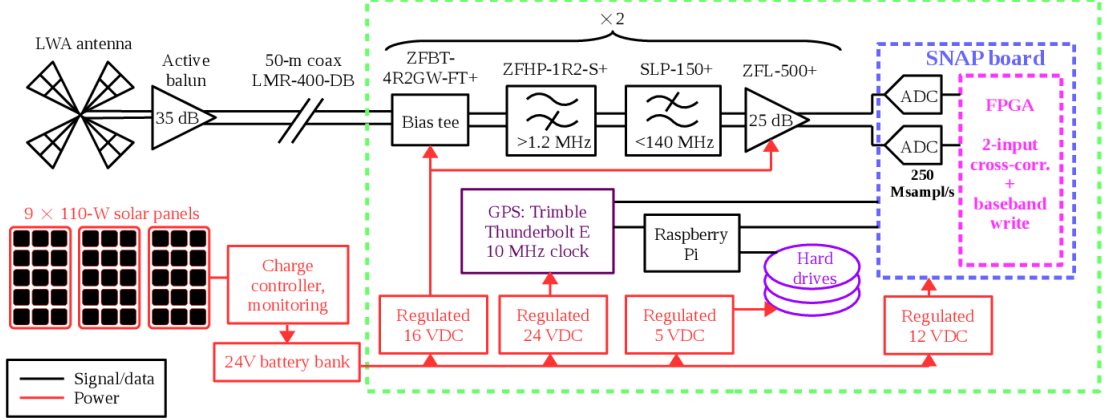


Figure 3.9: Autonomous station single-antenna block diagram. A dual-polarization LWA antenna, fitted with an active front-end balun, connects to the back-end readout electronics through 50 m coaxial cables and is housed in a green dashed Faraday cage box. A second-stage electronics chain consisting of filters and further amplification allows the two antenna signals to pass through. An on-board FPGA is built-in on a SNAP board that measures channelized baseband and spectra from both inputs and digitizes the signals at 250 Msamp/s. The SNAP board is controlled by a Raspberry Pi, and the baseband data and spectra are obtained. Baseband data are stored on the external hard drives. Solar panels charge a 24-V battery bank, which powers the system.

generated from the charge controllers and other switching components. Thus, a solar power system solution was implemented on the first autonomous station to run the system autonomously continuously. Total power experiments like PRI^ZM are more susceptible to RFI; consequently, a manual charging method is used.

During the relief voyage, the installation process included mechanical assembly and alignment of the antenna structure, laying coaxial cables, installing three solar panel mounts (with three panels each, for a total of nine panels), and installing a small processing hub consisting of a plastic bin housing the readout electronics, two batteries, and power control electronics. The first autonomous station signal chain shown in Figure 3.9 was installed in April 2019 at the hydroshack site ($46^{\circ}52.205'S$, $37^{\circ}50.612'E$) on Marion Island. The installation was the first step in testing the technologies required to create the full array. A similar antenna and front end active balun discussed in (§3.2.1 and §3.2.2) were used, and the back-end electronics and the power system are discussed in detail below.

3.5 Autonomous Station Signal Chain

For the autonomous station, the same LWA antenna and FEE are used. The hydroshack site was assessed to avoid installing the hardware on top of a mire, and we were able to spot even terrain and were suitable for installing our hardware. The hydroshack site is a reasonable hiking distance from the main base, yet sufficiently far to reduce base-generated RFI.

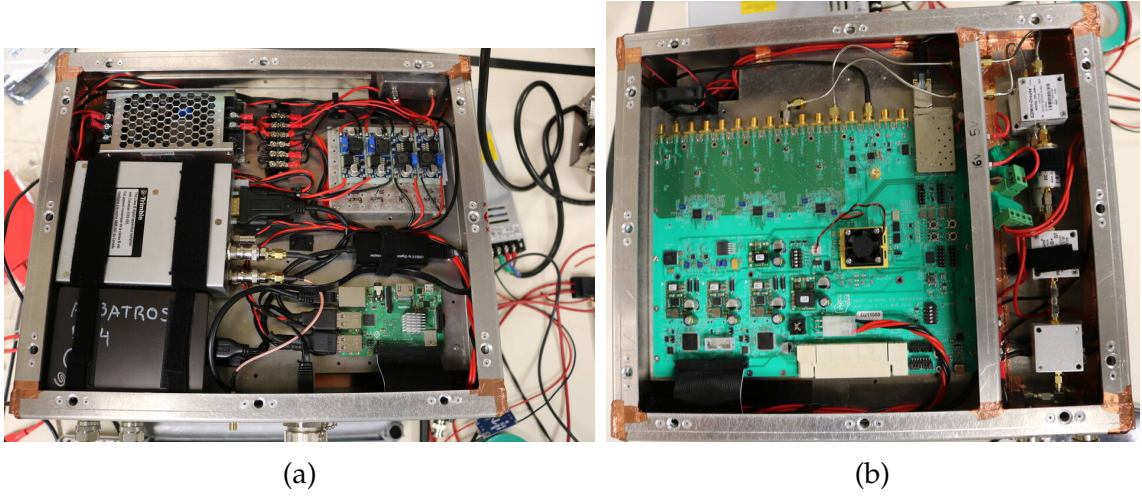


Figure 3.10: (a) One side of the mounting plate with visible power distribution circuitry is shown in the single autonomous station Faraday cage, Trimble Thunderbolt E GPS-disciplined clock module, external hard drives and RPi. (b) The analog signal chain mounted in the RF partition on the left and the SNAP board mounted on the right in the single autonomous station Faraday cage.

3.5.1 Back-end Electronics

The back-end electronics are very similar to those used for the 2-element pathfinder. However, a few key differences are external hard drives to store data and cross-correlate offline afterward and a Trimble Thunderbolt E GPS-disciplined clock module. Also, there were revisions done on the enclosure. The enclosure was a laser-cut, folded sheet metal design with captive quarter-turn fasteners to make it easier to assemble and more field-friendly.

The Faraday cage shown in Figure 3.10a and denoted by the green dotted line box in Figure 3.9 is located 50 m away from the antennas. The analog signal chain shown in Figure 3.10b consists of a pair of high- and low-pass filters (Mini-Circuits ZFHP-1R2+ and SLP-150+) that together band-limit the signal to 1.2 MHz to 140 MHz, and after the filters is the Mini-Circuits ZFL-500+ amplifier with a 25 dB typical gain. The amplifier that I selected is the new change with respect to the 2-element pathfinder. The amplifier operates at a frequency range of 0.05 MHz to 500 MHz which is well within our desired frequency range. An AWR simulation shown in Figure 3.11 shows the plot of a combination of S21 magnitudes in dB of the low pass filter, high pass filter, and the amplifier. It clearly shows that the cutoff frequency is \sim 150 MHz corresponding to the \sim 24 dB magnitude in dB. The autonomous station signal chain response is flatter with higher gain, as shown in Figure 3.12.

In comparison to the two-element pathfinder, the cut-off frequency of the low-pass filter increased from 81 MHz to 140 MHz to capture downlink signals at 137 MHz to 138 MHz from the ORBCOMM satellite constellation. The ORBCOMM signals are beneficial to the final ALBATROS array because they provide a convenient means for synchronization across the antenna stations, serving as a backup to the GPS timing discussed below. Actual lab tests recommend that on time scales of \sim 30 s, relative timing between various autonomous stations can be estimated to a precision of better than a couple of tenths of a nanosecond utilizing

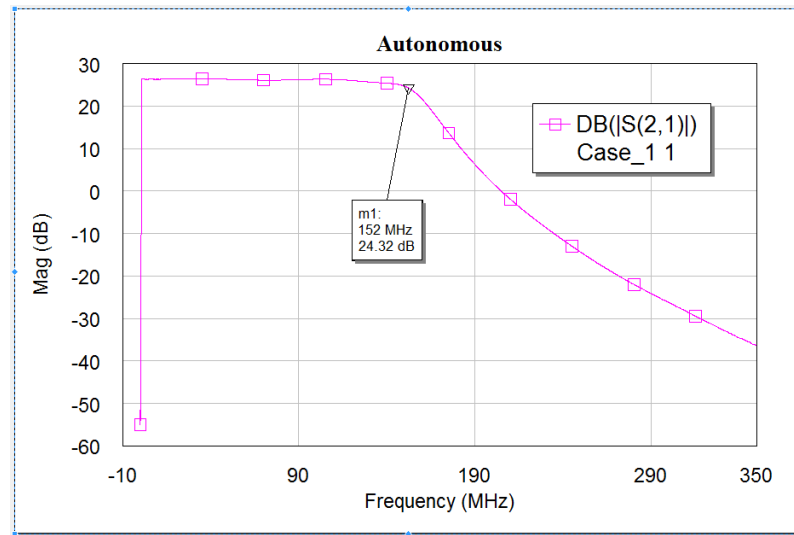


Figure 3.11: Autonomous station analog chain response. The plot is a combination of the S21 magnitudes in dB of the low pass filter, high pass filter and the amplifier. It shows that the cutoff frequency is ~ 150 MHz corresponding to the ~ 24 dB magnitude in dB.

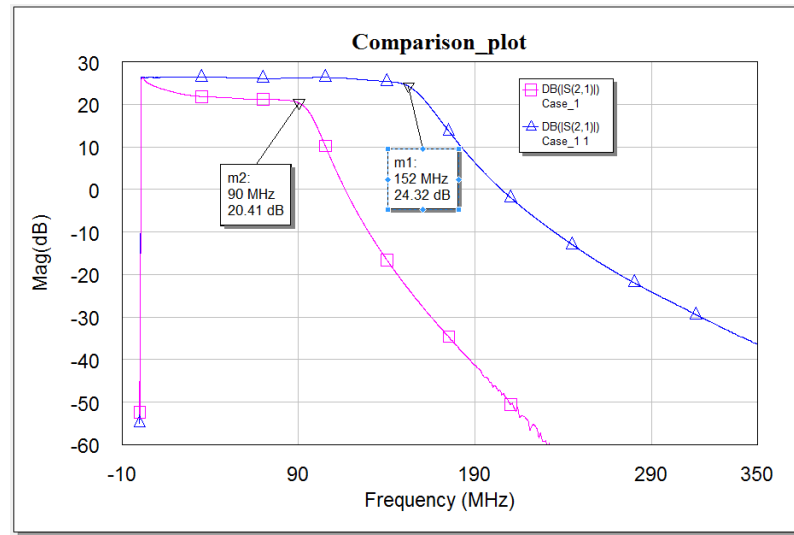


Figure 3.12: The comparison of the pathfinder and autonomous station analog chain response. The autonomous station signal chain response in blue is flatter with higher gain compared to the pathfinder response in pink.

ing a solitary satellite. At 10 MHz the correlation phase error is $\lesssim 1^\circ$. With open-access orbits and various satellites commonly within the field of view, the ORB-COMM baseband data supposedly saved simultaneously with the astronomical data can provide offline synchronization of the ALBATROS stations. Since the ORBCOMM and science data are recorded simultaneously by the same system, enhancement to the timing calibration can be applied in post-processing.

The signals are then digitized at 250 Msampl/s by the SNAP board mounted in the Faraday cage in Figure 3.10b. A Trimble Thunderbolt E GPS-disciplined clock module creates a 10 MHz reference that is locked from the SNAP board internal ADCs. The reason for phasing out a Valon was because of its wide frequency band and having limited applications. A Trimble Thunderbolt E GPS-disciplined clock module replaced the Valon for high volume synchronization applications. The SNAP board FPGA processes channelized baseband data for every polarization over tunable frequency windows inside the 0 MHz to 125 MHz range, with the options of 1-, 2-, 4-bit baseband channelization, and auto-and cross-spectra from the two polarizations over the full 0 MHz to 125 MHz range, collected more than few-second spans. As we are doing long term observations, 1-bit channelization enables us to store data without running entirely out of external hard drive space. However, the auto spectrum information cannot be recovered from 1-bit data. The appropriate transition levels must be tuned/set for 2- and 4-bit quantization. Hence, the higher the number of bits, the higher the signal fidelity and the higher volumes of data.

The decrease in bit profundity happens simply after the SNAP board has channelized the baseband, and the cross-channel spillage (due to, e.g., RFI and inclines in RF power as observed by the ADCs) is this way unaffected by the low bit profundity. A polyphase filter bank (PFB) is used in the FPGA firmware to do the channelization. The incoming analog signal passes through a polyphase filter bank after being sampled by the ADC. The PFB module supports out-of-band signal suppression and also generates a flat response across the channel.

A SNAP board is controlled by the RPi 3B+ and gets the auto-and cross-spectra through GPIO pin connections, and the spectra are saved to an on-board SD card. The baseband data is passed through an ethernet from the SNAP board to the RPi and saved to external hard drives. The presentation of gigabit ethernet with the RPi 3B+ model has empowered the high data throughput related to writing baseband. As a benchmark, 1-bit baseband recording of two polarizations more than 10 MHz of transmission capacity yields an approximate data rate of 5 MB/s or 400 GB/day, and 4-bit baseband recording will result in even higher data storage capacity. Currently, a human needs to go to the autonomous station site to copy data and exchange hard drives, which has resulted in the development of the USB multiplexer. The multiplexer switches the drives' 12 V and 5 V supplies, guaranteeing that unused drives will not consume any power. One multiplexer can only take up to 8 hard drives. Therefore two multiplexers will be used to accommodate 16 hard drives as specified. The largest and cheapest hard drive capacity available is 8 TB; consequently, the minimum capacity being considered for each autonomous station is 128 TB. The other autonomous station deployment sites are further away from the main base, hence developing a hard drive bank.

Module	Power Dissipation (W)	Voltage (V)	Current (A)
SNAP board	~30	12	2.5
FEE and Dual Pol	~8	16	0.48
2nd Stage Amplifier	~2.4	15	0.16
Trimble	~12	15	2.4
RPi	~12.5	5	2.5
Disk Drive	5-10	5/12	1-2
Total	~70		~9

Table 3.2: The ALBATROS system ratings. The figures shown are from the datasheets of the various components and considering that the antennas are dual-polarization antennas.



Figure 3.13: (a) The three supporting structures for the nine solar panels mounted on a rigid metallized plastic panels. Behind the supporting structures is the plastic enclosure housing the readout electronics, two batteries, and the power control electronics. (b) Interior of the plastic enclosure housing the readout electronics, two batteries, GPS antenna, and the power control electronics

3.5.2 Solar Power Supply System

The future autonomous stations shown in Figure 3.7a are farther from the island's main base, hence, the development of autonomous power supply systems. A solar power supply system was developed for the first autonomous station installed at the hydroshack site. The system is powered using an array of nine SunPower SPE-E-Flex-110 solar panels that charge a 24 V battery bank made up of two series-connected, 12 V, deep cycle, lead-acid batteries. A single solar panel has a nominal power of 110 W, capable of producing an open circuit voltage of approximately 22.8 V and 6.3 A. On account of the extremely incessant cloudy conditions on Marion Island, the charging capacity of 1 kW is deliberately immense for the required ~ 70 W to run the station. Table 3.2 shows the power budget for the ALBATROS autonomous station. The system was designed for worst-case operation at the winter solstice, with extra power generating capacity so that batteries will be depleted only in relatively extreme cases and can recover quickly.

The nine solar panels' supporting structures were specifically designed to

manage the gale-force winds on Marion Island. However, it was challenging to install them as the volcanic ground minimizes the appropriate anchoring ability. With Marion being an environmentally protected base, there are additional limitations on the type of anchoring hardware that can be used. Wind power was one of the available options. Marion has an ornithology research group, and it is environmentally protected; wind power infrastructure was not going to be accepted as it was going to attract the birds. The material used for the three mounting structures was the t-slotted extruded aluminum framing. All joints were designed to be adjustable to accommodate the uneven terrain and allow varying incline angles. Each of the structures carries three solar panels mounted on a rigid metalized plastic panel. The structures are oriented due north and are designed to incline the solar panels at a relatively steep angle to perform efficiently under winter conditions. The three supporting structures with mounted solar panels are shown in Figure 3.13a. Behind the supporting structures is the plastic enclosure housing the readout electronics, two batteries, and the power control electronics shown in Figure 3.13b. The plastic enclosure is a Mpact 528H, made of rugged weatherproof plastic, modified to include a hinged lid and cable feedthrough points. The feedthrough points were stuffed with brass scouring pads and sealed with a metal mesh cloth to prevent mice from entering. Each group of solar panels mounted on three structures is connected in series. The three groups' three connections are connected parallel to the Victron BlueSolar MPPT 150|35 charge controller, optimizing power transfer from the solar array when charging is required. Monitors charge level reducing output current when the battery bank is fully charged. An Arduino logs the data from the Victron charge controller to an SD card and switches power on and off to the readout electronics box. The on/off feature is compulsory to avert battery system damage from intense discharge. Typically, for lead-acid batteries, the battery should never be discharged down to 0 % state of charge, and ideally (to preserve battery cycle life) never or seldom below 50 %. The system also has a battery power conservation feature, which schedules observations for distinct periods, often during the night when ionospheric conditions are more favorable. For the time being, observations were continuously done while the system is in engineering mode, but this feature will be used in the future to keep the data volume manageable. The power logging and control system, the Victron charge controller, and an EMI filter are housed together in an aluminum box shown in Figure 3.14. The solar charge controller generates RF noise, which would likely cause interferences; hence, an EMI filter was designed to minimize conducted emissions on the solar charge controller's photovoltaic side. Figure 3.15 shows the complete installation of the first autonomous station. Thus far, the hydro shack installation was the first and only fully autonomous station deployed on the island. Additionally, baseband-ready readout boxes are used with the 2-element pathfinder at the PRI^ZM site. The only missing aspect of Junior's setup is the power autonomy, but there is the capability to record baseband from both Junior's and hydro shack at the same time.

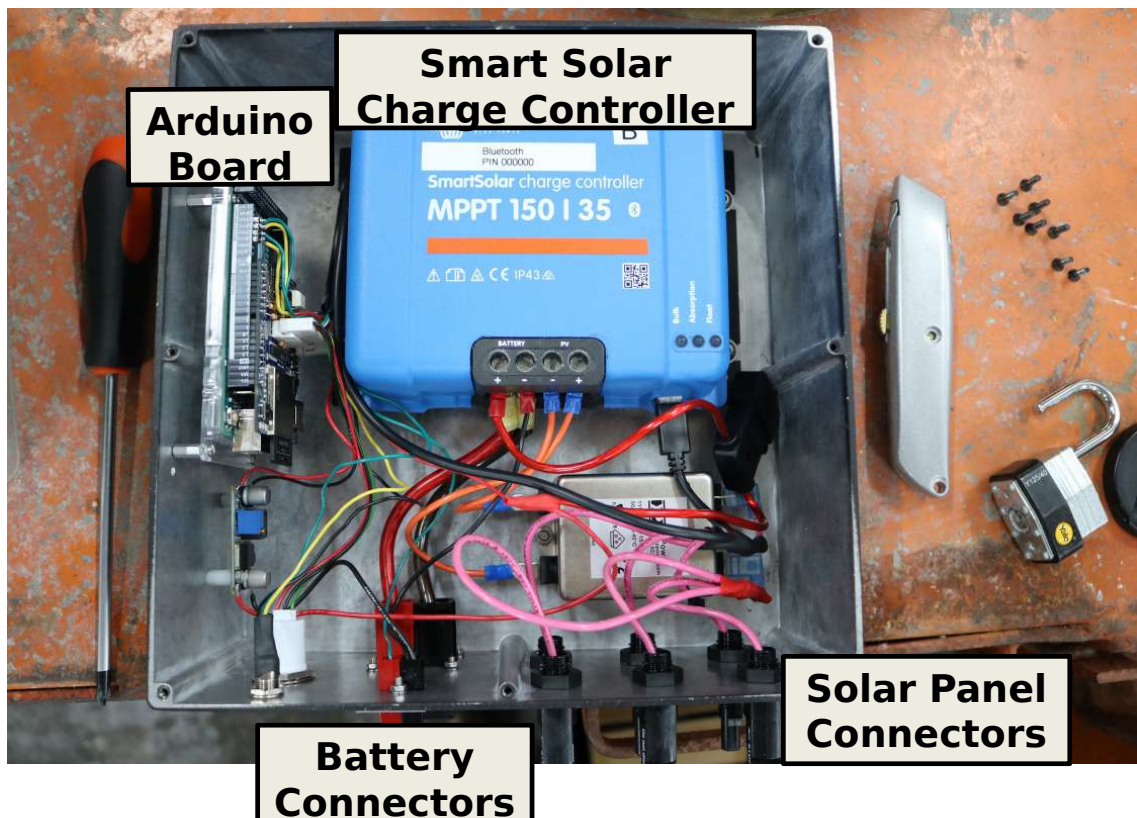


Figure 3.14: An aluminum box houses the power logging and control system, the Victron charge controller and an EMI filter.

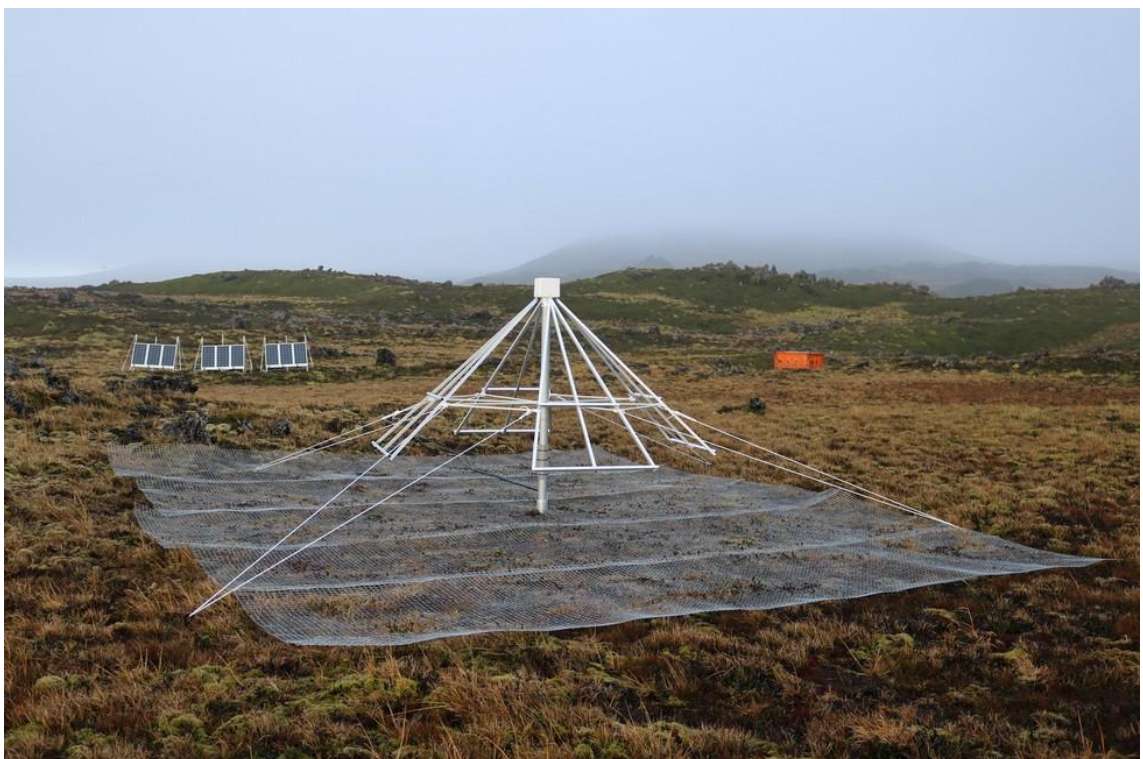


Figure 3.15: April 2019 deployment of the first ALBATROS autonomous station was a success. The mounted solar panels and the LWA antenna are visible. The hardware for the first autonomous station was enclosed in the orange container, and it was only present temporarily during the takeover period.

Chapter 4

PRI^ZM Instrumentation

4.1 PRI^ZM Experiment Overview

PRI^ZM [Philip et al., 2019] shown in Figure 4.1 is an experiment that is specifically designed to study cosmic dawn in the universe using total power measurements of the global 21 cm signal from neutral hydrogen, redshifted to 30 MHz to 200 MHz. The experiment consists of two compact, modified four-square antennas [Jáuregui-García et al., 2017] that operate at central observing frequencies of 70 and 100 MHz. The combined frequency range of both antennas spans 30 MHz to 200 MHz, which brackets the predicted absorption feature from cosmic dawn. Figure 4.2 shows the subsystems of PRI^ZM which will be discussed briefly, followed by a discussion on revised subsystems. The first installation of PRI^ZM in Marion Island was in 2017, and over the years, there have been incremental upgrades and maintenance to the front and back end electronics. My main contribution was making additional upgrades that were planned to field during the 2020 Marion takeover voyage, which unfortunately did not happen because of the COVID-19 restrictions.

4.2 Signal Chain

4.2.1 Antenna

Figure 4.2 shows the original 2017 configuration of the signal chain for a single polarization of the PRI^ZM antenna. The antenna design was initially developed for Sonda Cosmologica de las Islas para la detección de Hidrógeno neutro (SCI-HI), which was deployed in Guadalupe Island (200 km off the coast of Mexico) in 2013. The antenna is made up of four petals that form a pair of crossed dipoles.

Each petal has three trapezoidal facets angled at various angles with respect to the ground. The angles were selected to minimize spectral variation in the beam shape. The antenna beam pattern's width has a direct dependence on the angles of the trapezoidal facets, and the height of the antenna above the ground changes the beam symmetry [Voytek et al., 2014]. The PRI^ZM antenna structure was redesigned with respect to the original SCI-HI design to survive the high winds on Marion Island, as shown in Figure 4.3.

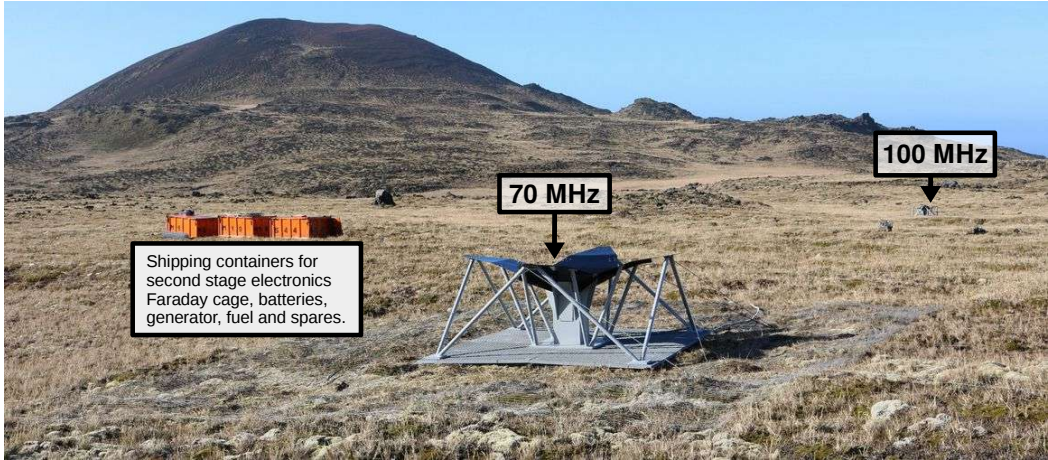


Figure 4.1: The PRI^ZM experiment built on Marion Island. The two antennas (70 MHz and 100 MHz) are visible and the three shipping containers enclose the second stage electronics Faraday cage, generator, batteries, fuel, and spares. The main base lies four kilometers away from the observing site.

4.2.2 First Stage Electronics

The first stage electronics are housed in the column supporting the antenna petals as shown in Figure 4.4, and the block diagram of the first stage electronics is shown in Figure 4.5. The signal from each single-polarization PRI^ZM dipole is fed to the calibrator switch by a coaxial cable, which is 200 mm long. In order to dissipate the current on the outer conductor of the coaxial cable, a ferrite core is used. The calibrator switch is required to switch between observations of the sky and the calibrator sources of $50\ \Omega$, which are connected to the switch input terminals. Two cascaded WEA101 LNAs are used to amplify the selected signal at the switch output. Additional electronics in the first stage electronics box include voltage regulation circuitry for LNAs and temperature sensors. The two main improvements are upgrading to a latching switch from the 2017 to 2018 version, adding the noise source, and spreading thermometry through the components shown in Figure 4.5.

4.2.3 Second Stage Electronics (SSE)

A custom-designed Faraday cage (Figure 4.8) that encloses the SSE is housed in one of the shipping containers shown in Figure 4.1. The signal from the first stage electronics is fed via a $\sim 50\text{ m}$ LMR400 coaxial cable, which is a reasonable distance to minimize the contamination from possible self-generated RFI. The coaxial cables are mouse-proofed using a few meters of stainless steel wire mesh cloth wrapped near the cable penetration points. The multi-tiered interior of the Faraday cage ($\sim 300\text{ mm} \times 470\text{ mm} \times 240\text{ mm}$) is shown in Figure 4.7 with the top panel removed. The readout box services both antennas. There is a separate readout chain for each antenna, but the housekeeping and switch control electronics are shared between the antennas. There are two central shelves for mounting the SNAP board and RPis. Each SNAP board services each antenna, and one RPi controls each SNAP. A third RPi is shared amongst the two SNAP boards for housekeeping purposes.

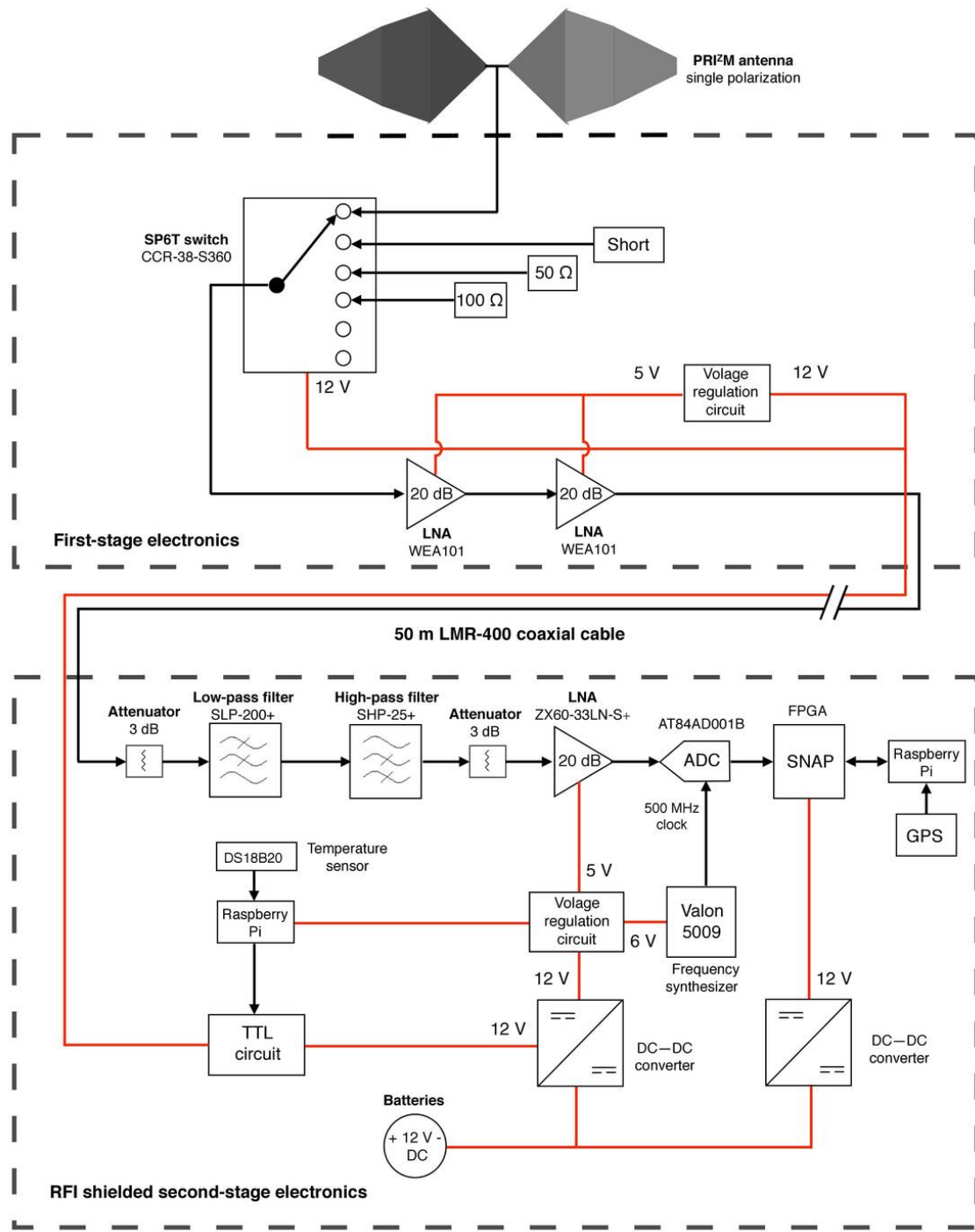


Figure 4.2: PRI^ZM antenna block diagram for a single polarization. The upper and lower dashed boxes denote the electronics chain's first and second stages. To decrease self-generated RFI leakage, the two stages are separated by 50 m [Philip et al., 2019]



Figure 4.3: A completed 100 MHz antenna mounted on a $2\text{ m} \times 2\text{ m}$ fibreglass grating with the approximate dimensions $\sim 3\text{ m}$ on a side

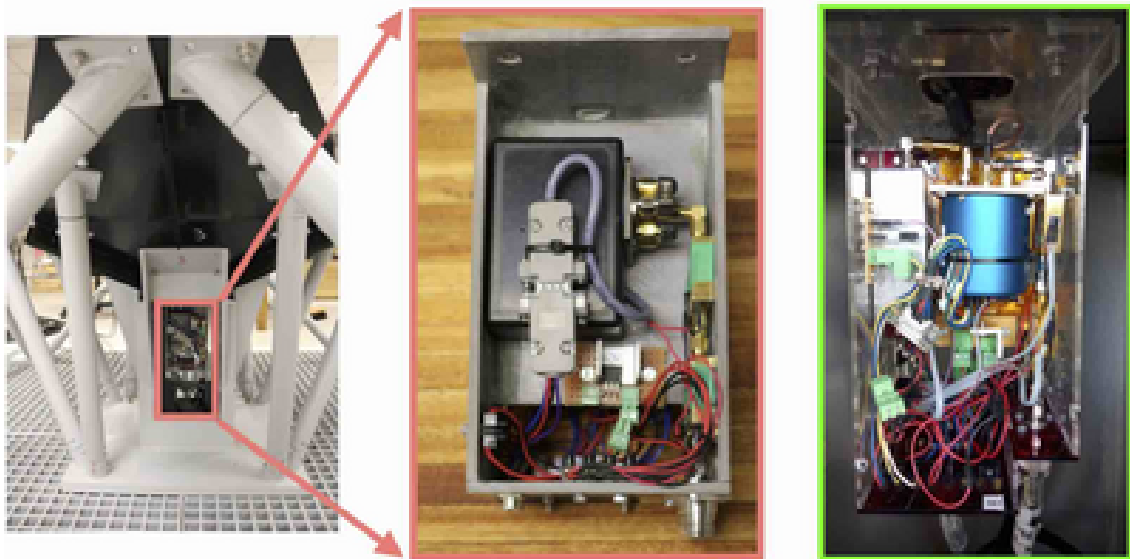


Figure 4.4: The electronics box for the first stage. Shown in pink is the original installation from 2017 and green shows the 2018 upgrade which is currently installed in the central column under the antenna.

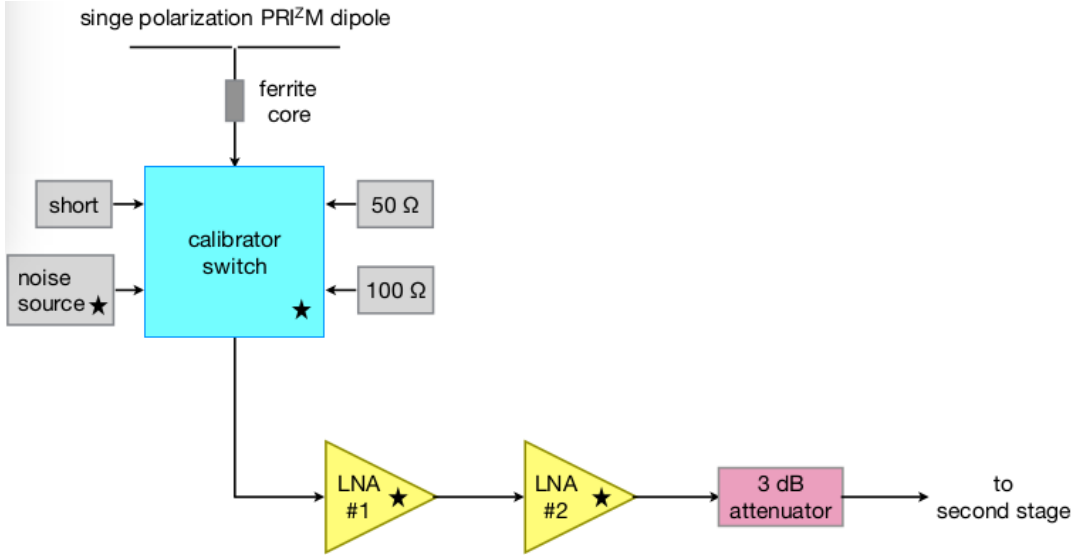


Figure 4.5: A simplified schematic of electronics from the first stage. The schematic reflects the 2018 configuration. Components marked with a star are outfitted with one-wire digital temperature sensors.

The filtering and amplification stage is applied to each polarization from each antenna. It consists of Minicircuits SLP-200+ and SHP-25+ low and high pass filters that band limit the RF signal to 30 MHz to 200 MHz. The filtered signal is amplified by 20 dB using a Minicircuits ZX60-33LN-S+ amplifier. The output signal is then fed to the readout electronics.

Each SNAP board receives the two RF signals from the two polarizations of a single antenna and samples the signals at a rate of 500 Msamp/s using a dual, monolithic, eight-bit, AT84AD001B external analog-to-digital converter (ADC) that is connected to the SNAP board via a Z-Dok connector. A Valon 5009 frequency synthesizer provides the ADC with a clock signal. The SNAP board employs a Xilinx Kintex 7 FPGA to compute auto- and cross- spectra from and between the four inputs, with 4096 frequency channels spanning 0–250 MHz. An RPi controls the SNAP board and saves data to an onboard SD-card. The RPi's timing is provided by an Adafruit Ultimate GPS module connected to an external active GPS antenna.

The SSE box also encloses the additional hardware that controls the calibrator switch states and voltage regulation. Figure 4.6 shows the schematic of the switch control circuit. The L298 full-bridge drivers were used to make the control circuit, and the transistor-transistor-logic (TTL) is used to generate the control signals. Five L298 high-current full-bridge drivers are used to provide the reset and actuation signals. A power MOSFET is used to turn on and off a noise source in the FSE box. A RPi controls the logic gates of the integrated chips. The whole first stage electronics is temperature monitored using the 1-wire DS18B20 temperature sensor.

The main power to the SSE box is fed via a BNC connector. The SSE box houses the two DC-DC converters on the bottom layer, which both provide 12 V output, two SNAP boards are powered with 12 V from one DC-DC converter. There are additional power regulators that input the 12 V from the other DC-DC converter to supply lower voltage levels to multiple components in the system.

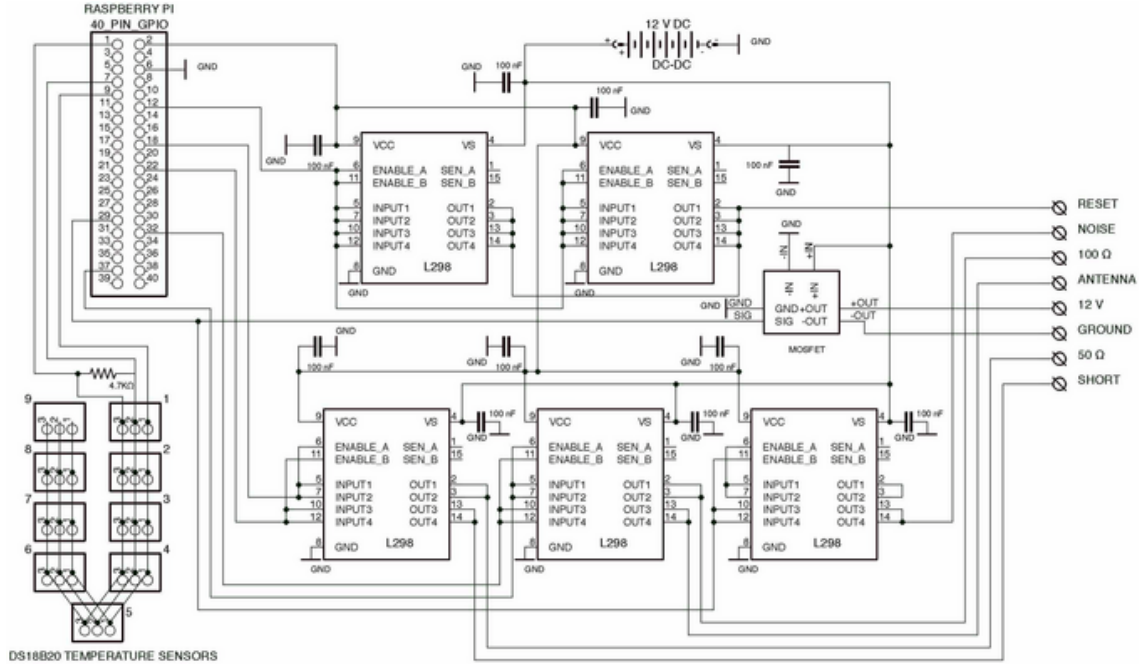


Figure 4.6: The schematic of a switch control circuit. The L298 full-bridge drivers were used to make the control circuit. The two top drivers provide the reset signals, and the three bottom drivers provide actuation signals. To turn on and off the noise source in the FSE box, a power MOSFET is used. Nine 1-wire DS18B20 temperature sensors monitor the temperature.

4.2.4 Power

The PRI^ZM system is powered using eight 12 V 200 A h battery bank wired in parallel as shown in Figure 4.9. The total system draws \sim 65 W when the batteries are fully charged, the system can operate for approximately one week. Battery charging is performed manually using a Honda EU30is generator, and a fuel cache kept at the observing site. The batteries are connected to two DC/DC converters during observations. The DC-DC converters are enclosed in the SSE box and provides stable voltage outputs despite the slow decline of the battery voltage. Further regulation is performed to supply power to several components in the system.

4.3 Revised PRI^ZM Instrumentation

This section describes revisions made to some of the PRI^ZM subsystems in preparation for the 2020 voyage to improve functionality and performance. The first stage, electronics enclosure redesign, will be discussed in the next subsections and the revised SSE enclosure. Due to COVID-19 restrictions, the redesigned first stage electronics and SSE were not fully integrated and tested, and this section reports the work that was completed before lockdowns began. The 2020 Marion voyage was canceled because of COVID-19¹.

¹<https://www.timeslive.co.za/news/south-africa/2020-04-06-sas-expedition-to-marion-island-downsized-over-coronavirus-fears/>

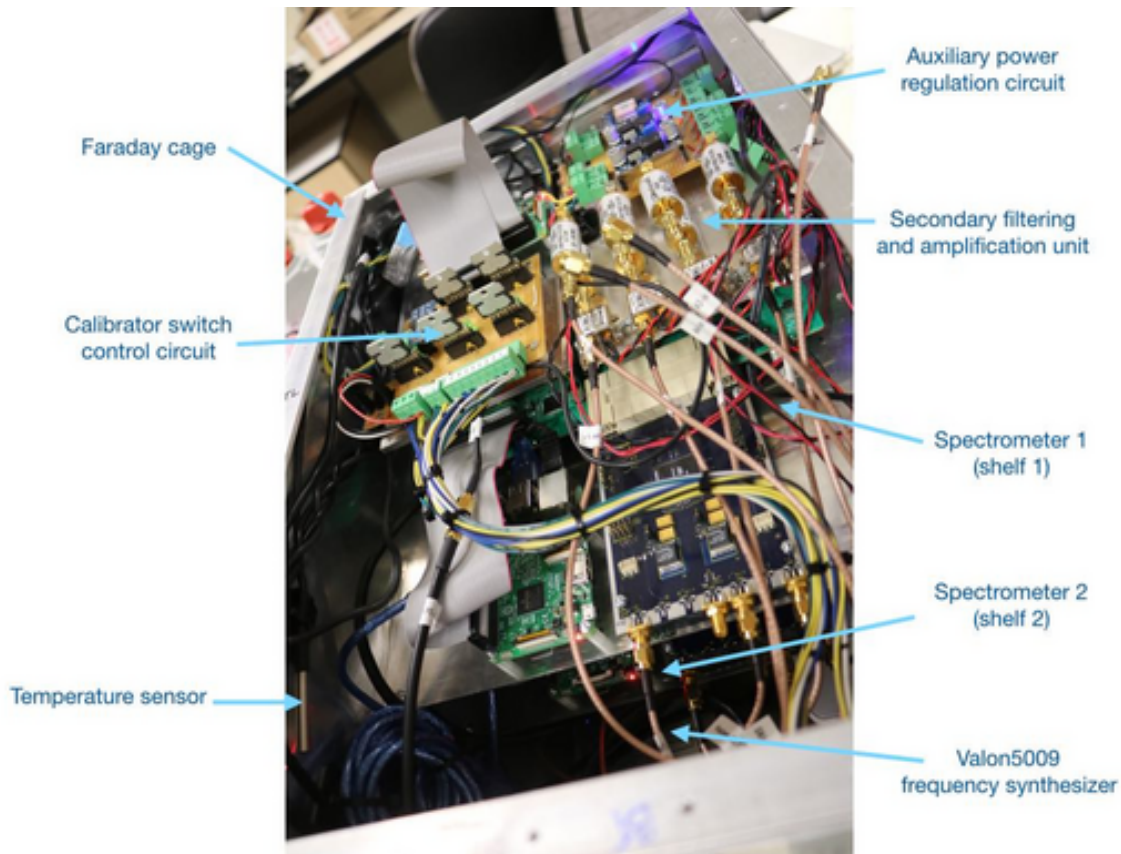


Figure 4.7: The multi-tiered interior shown while the SSE box top panel is removed. Most of the internal components in this configuration can be accessed, but one more panel needs to be opened to access the DC-DC converters.



Figure 4.8: The SSE Faraday cage made with separate brackets and flat sheets.

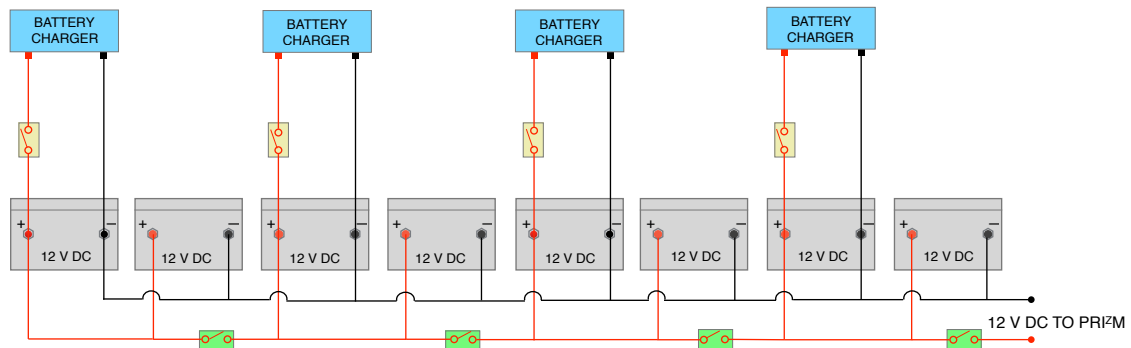


Figure 4.9: PRI^ZM's power distribution chain consists of eight 12 V 200 A h lead crystal batteries each. The batteries work in pairs that, through the green switches, are cascaded together. The battery pairs are disconnected during charging, and a single battery charger charges two batteries simultaneously. To connect the battery chargers, yellow switches are used. All yellow switches are turned OFF during the observation, and all green switches are powered ON.

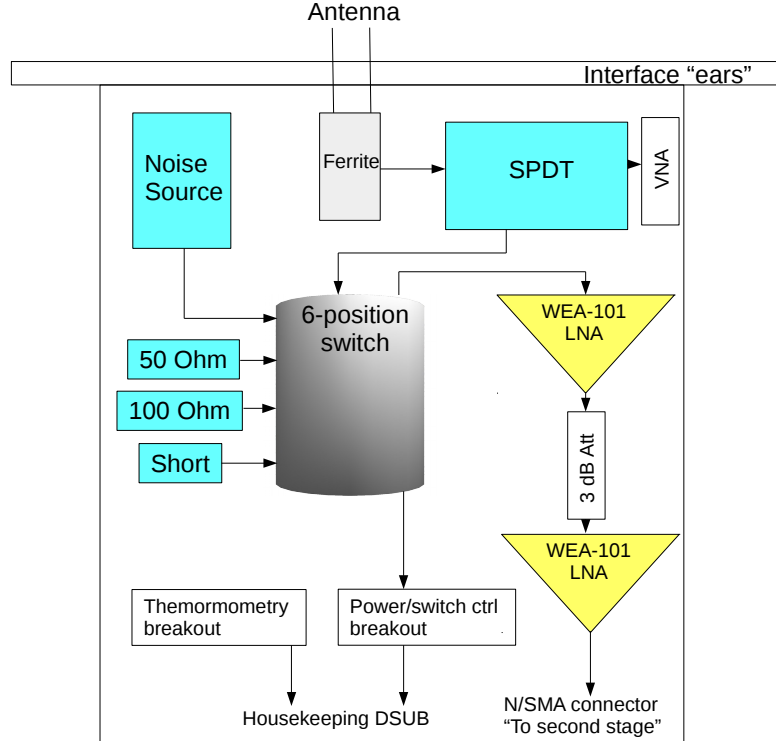


Figure 4.10: The block diagram of the proposed FSE architecture showing the 6-position switch connections, the breakouts for housekeeping, SPDT for controlling the SP6T and amplification. The VNA is not permanently installed, and the box drawn indicates a connection point.

4.3.1 First Stage Electronics (FSE)

A new FSE and enclosure were proposed for the 2020 deployment. Figure 4.10 shows the block diagram of the proposed FSE architecture. Off-the-shelf enclosures were used instead of the previous enclosures' custom geometry, and these new boxes provide slightly more room to house the SPDT switches, which are new additions. To ensure that the enclosure would accommodate all the FSE, dummy placeholder components were crafted and placed in the enclosures. Figure 4.11 shows a nominal component layout. The perforated gray sheet serves as a mechanical breadboard for easy addition of new parts without drilling the enclosures. Two enclosures are attached back to back to service the two polarizations. Most of the housekeeping electronics are on the side of Figure 4.11, which is intended to be accessed from the east-facing column door, giving the human slight shelter from the prevailing wind. The only housekeeping breakout on the second enclosure is half of the one-wire thermometry bus.

The new box currently accommodates only one SPDT switch per side, and the plan is to add more switches to facilitate additional VNA measurements. The single SPDT switch does allow us to do VNA measurements of the antenna without disconnecting the antenna cables. The antenna cables connect the PRI^ZM dipole to the calibrator switch. A right-angle adapter will be required on the SPDT to interface with the antenna cable. Without the SPDT switch in place, the S11 measurement looking into the antenna requires the antenna cable's physical disconnection from the 6-position switch. The new SPDT switch enables a selection of

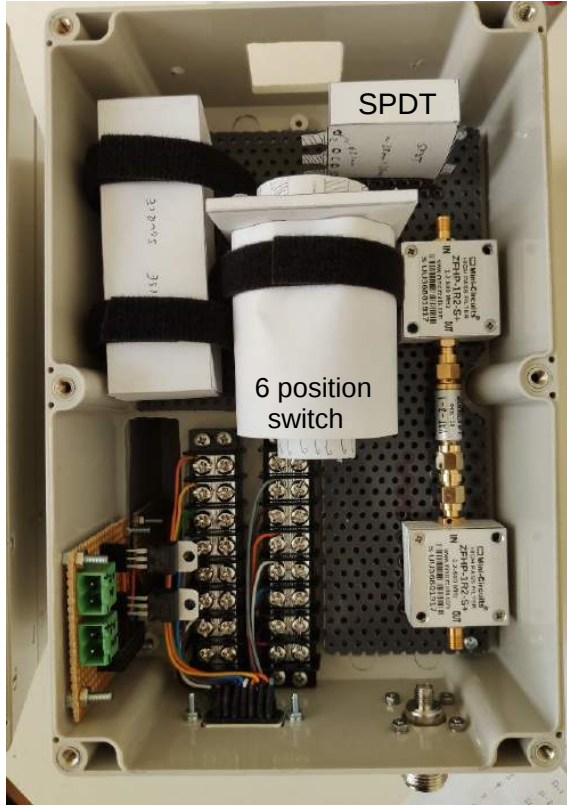


Figure 4.11: General layout of the components in the proposed FSE enclosure with dummy placeholders.

two positions, unlike the current PRI^ZM configuration where the antenna signal is fed through the 6-position switch. The SPDT either selects the antenna signal to divert through the SPDT switch for VNA connection or continue as in the current configuration. In the new configuration, there is a free SMA port on the SPDT where the VNA can be connected or disconnected for measuring S11 looking into the antenna without connecting or disconnecting the cable.

The terminal blocks for power and housekeeping signals have 16 positions total, so one is unused by the DB-15 breakout (and the SP6T switch can block the unused position). The filters in Figure 4.11 are placeholders, but they are about the same size as the WEA-101 LNAs highlighted in yellow in Figure 4.10. In Figure 4.12, the incoming DB-15 connector is split out into two terminal blocks, and Table 4.1 shows the connection configuration. The wall-mounted PCB has a 12V input and provides the LNAs with a 5V output and the one-wire thermometers with a 3.3V onboard output. All thermometers servicing both polarizations are ganged together on a single bus, so the headers are split accordingly across the enclosure's two halves.

4.3.2 Second Stage Electronics

A revised Faraday cage for the SSE was designed using Autodesk Inventor Professional 2018, and the sheet metal box is shown in Figure 4.17. The enclosure was revised so that each antenna has its SSE box. There was no longer shared housekeeping RPi that binds the SNAP boards together. That was the main driver for

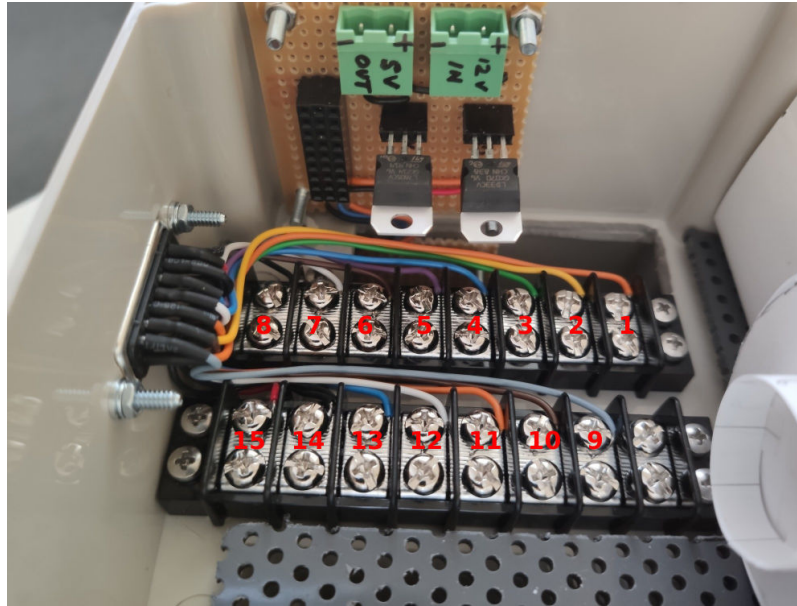


Figure 4.12: Housekeeping breakout. DB-15 pin assignments are annotated on the terminal blocks.

DB-15	Terminal Block	Colour	Function
1	L1	Orange	S1-1
2	L2	Yellow	S1-2
3	L3	Green	S1-3
4	L4	Blue	S1-4
5	L5	Purple	S1-5
6	L6	Brown	S1-6
7	L7	White	S1-Reset
8	L8	Black	Ground
9	R2	Gray	S2-Ant
10	R3	Brown	S2-Cal
11	R4	Orange	Noise
12	R5	White	Blank
13	R6	Blue	Temp Sensor
14	R7	Black	Ground
15	R8	Red	12 V

Table 4.1: Housekeeping pinout. Terminal block notation and numbering L and R denote left and right as viewed when the box is vertical, and numbers are from top to bottom. S1 denotes SP6T switch, S2 denotes SPDT switch.

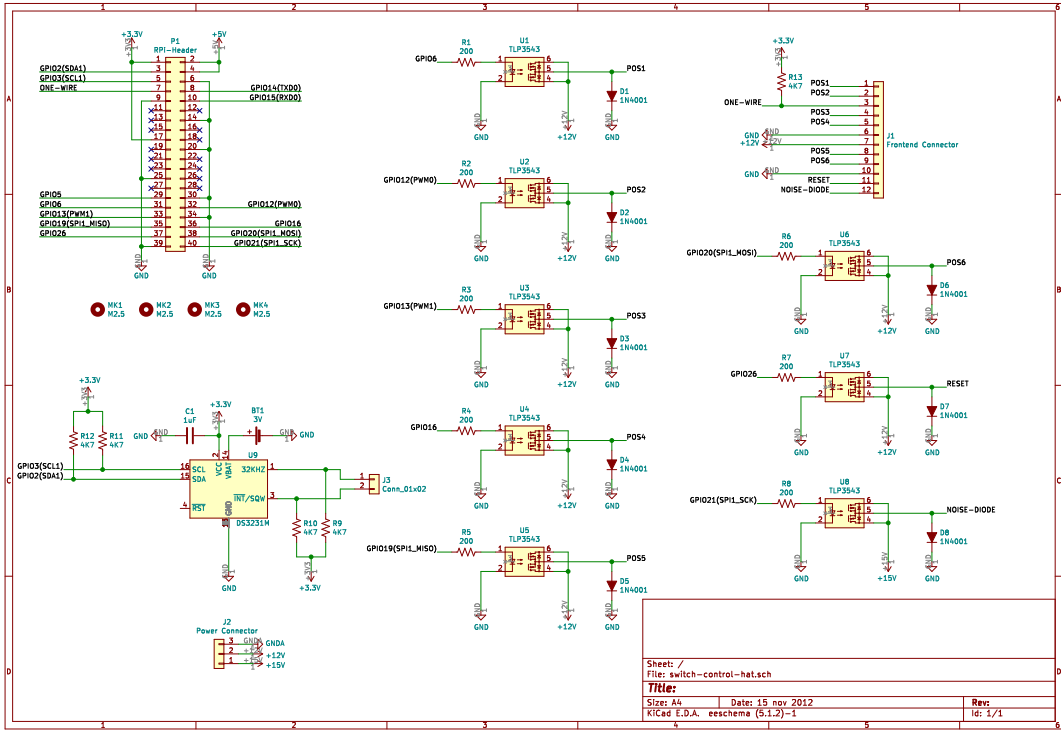


Figure 4.13: Schematic diagram of the newly designed switch control circuit. In the new design, six out of eight MOSFET output optocouplers are used to control the 6-position switch, and the other two are used for reset and noise source. The circuit has a built-in RTC. RPi's GPIO pins are connected to the RTC and the optocouplers to controls the functionality.

separating the SNAP boards/ enclosures.

The switch circuit was redesigned as shown in Figure 4.13 by the schematic. Eight TLP3543 MOSFET output optocouplers were used to make the switch control circuit. Six of the optocouplers are used to control the 6-position switch, one is used for the reset, and the last one is used for the noise source. The circuit is designed to have a built-in precision real-time clock (RTC), and the chip used is the DS3231. Figure 4.14 shows the 3D view of the switch circuit PCB. The bigger green connector connects to the FSE via a DB15 connector mounted on the enclosure's front panel, and the smaller connector is for power distribution. Figure 4.14b shows the female header, which is plugged directly into the RPi to form a stackable layout. The four mounting holes are precisely the same dimension as those of the RPi to fasten both of them simultaneously.

The main improvements to the new enclosure are listed below.

- Increased and improved accessibility of all components. Because each enclosure now services only one antenna, all components can be accommodated on a single shelf that can be accessed from both sides.
- The design is folded laser cut sheet metal, unlike the separate brackets and flat sheets that make up the current design
- Easier and cheaper to assemble and manufacture

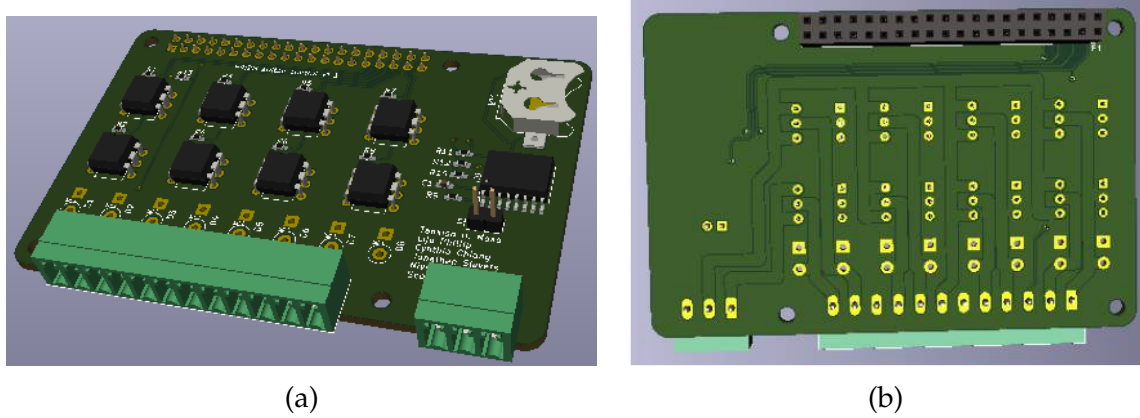


Figure 4.14: Top and bottom view of the newly designed switch control circuit. **(a)** Top view. In the new design, six out of eight MOSFET output optocouplers are used to control the 6-position switch, and the other two are used for reset and noise source. **(b)** Bottom view. The female header is connected to the GPIO pins of the RPi to form a stackable layout. The four mounting holes are exactly the same dimension as those of the RPi to fasten using taller fasteners.

- User-friendly (the holes are already in place to tap and screw the components in place, and the lids are fastened using captive quarter-turn fasteners).
- It was designed to fit into a hiking backpack for easy carrying when hiking to the PRI^ZM site. The current enclosure servicing both antennas is too large to carry on a hike to the site conveniently. The designed enclosure is $\sim 400 \text{ mm} \times 280 \text{ mm} \times 110 \text{ mm}$ and the current enclosure is $\sim 300 \text{ mm} \times 470 \text{ mm} \times 240 \text{ mm}$
- The new enclosure has a partitioned portion to accommodate the second stage RF electronics and ensure isolation from self-generated RFI from switching electronics elsewhere in the enclosure, as shown in Figure 4.15.
- A cooling fan was added to prevent thermal shutdowns of the SNAP board as shown in Figure 4.16.
- The switch control circuit was revised, and it is a stackable layout so that it sits on top of the RPi and connects directly to the GPIO pins.
- The RF absorbing material (3M Absorbing materials) is useful to line in the enclosure to avoid internal bounces from the RF noisy components, such as clocks of the digitizer and the switching from power supplies. That way, RFI is attenuated before reaching the amplifiers and other sensitive parts.

A list of all components housed in the new enclosure is presented in Table 4.2 with the quantities required. The front panel has feedthrough connectors that feed the signals/power in and out of the enclosure, as shown in Figure 4.17. A non-isolated panel mount BNC connector is used to supply the main power to the box. Two N-F/SMA-F bulkheads (Amphenol 242163) are used for the second stage RF signals for both polarisations. Panel mount ethernet feedthrough (CONEC 17-101814) is for the data transfer between an enclosed RPi and the laptop. The filtered DB15 connector connects the FSE to the box.

Component	Quantity
Meanwell 12VDC supply (RSD-60G-12)	1
Terminal block for power breakout	1
Buck converter	2-4
Amplifier (ZX60-43-S+)	2
High pass filter (HP-25+ HPF)	2
Low pass filter (SLP-200+ LP)	2
SNAP board	1
Switch control circuit	1
Raspberry Pi 3, 3B+, or 4	1
Chronodot	1
Adafruit GPS module	1

Table 4.2: A list of components that are housed inside the redesigned SSE enclosure.

The enclosures were fabricated, and the sheet metal parts fitted together as designed, all the components were installed in the enclosures, and they fit the mounting holes that were already in place. COVID-19 lockdowns happened before dry-runs could be performed.

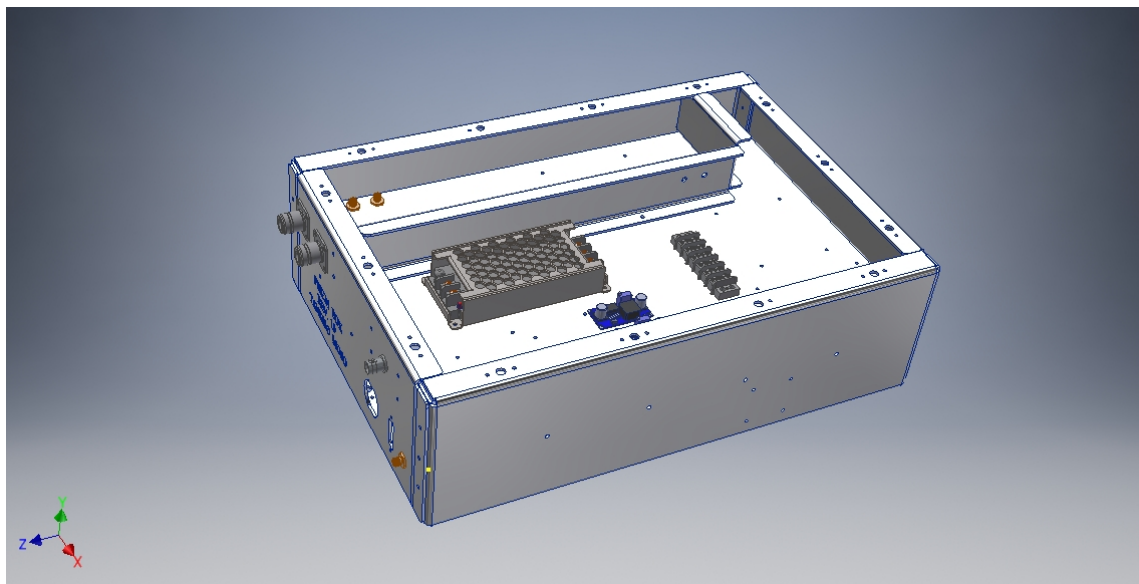


Figure 4.15: CAD of an enclosure with the top lid open. The partitioned portion is to avoid self-generated contamination from components with switching mechanisms. Some placeholders were mounted on the sheet metal design on Autodesk Inventor.

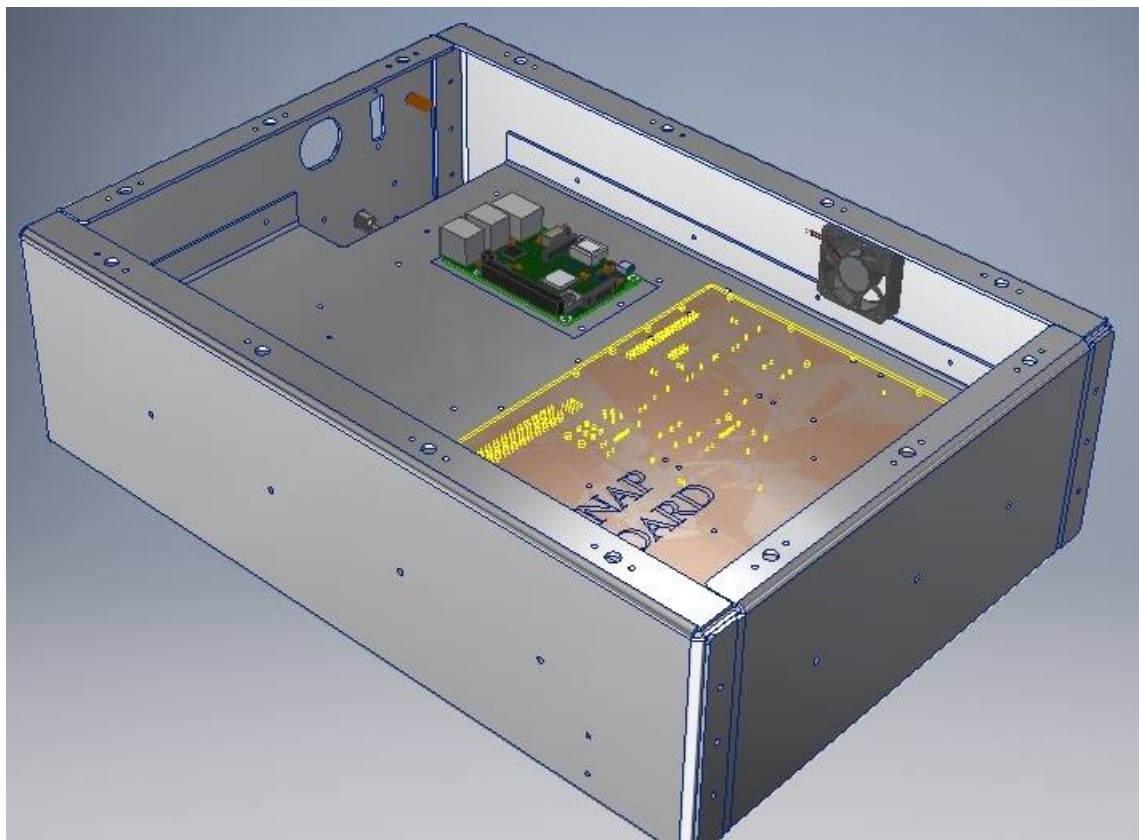


Figure 4.16: The bottom view without the lid, showing the SNAP board and its cooling fan, and the RPi.

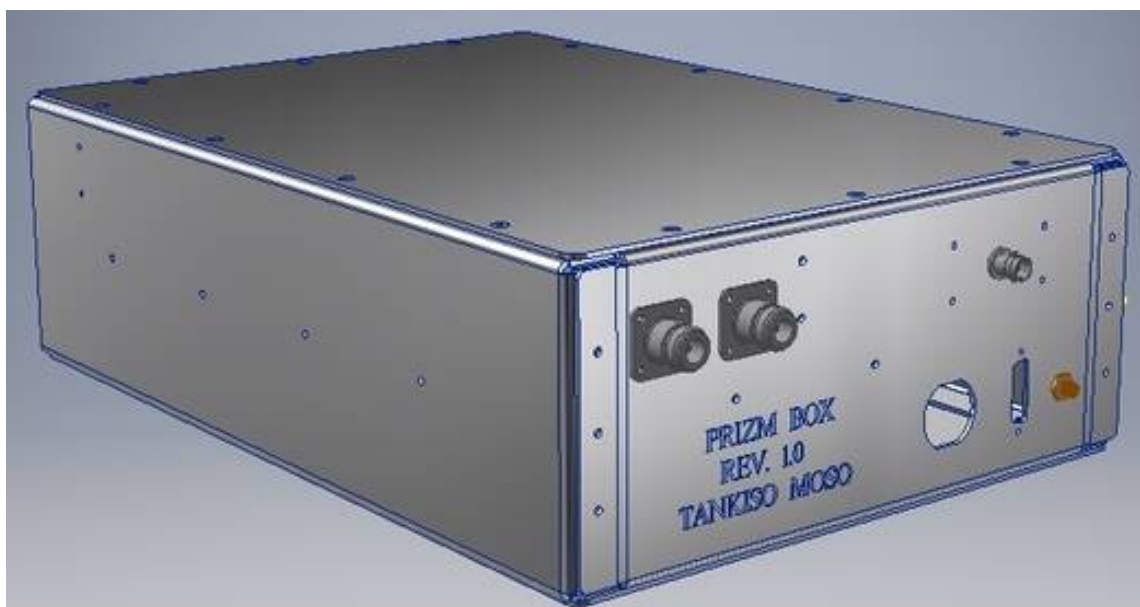


Figure 4.17: An enclosed box showing the connector placeholders and measured cutouts for other connectors that are not shown in this rendering

Chapter 5

Preliminary Data and Future Outlook

Figure 5.1 shows the results from the two-element interferometric array pathfinder discussed in §3.1. Figure 5.1 shows the auto- and cross- spectra where the waterfall plot was taken from one polarization over three days (June 18–21, 2018). The Galaxy rising/setting is visible in the structure. There are also ripples in frequency because of uncalibrated data, and the ripples arise from reflections in the cables. There is a qualitative difference between daytime and nighttime data, and this shows that the contamination from shortwave radio drops off significantly at night, when the ionosphere becomes quieter. It is distinctly visible from the figure that fringes show recurrent structure below ~ 10 MHz without data processing or data cuts. The auto spectra signal drop-off below $\lesssim 30$ MHz results from the combined response of the antenna and the front-end electronics as shown in Figure 5.2. These results demonstrate a proof of concept to proceed with the development of the autonomous stations.

An approximation of the instrumental consistency in gain can be obtained by comparing the total power between various days illustrated in Figure 5.1. Within the frequencies of 30 and 40 MHz, it has been discovered that the RMS gain variations are below 1 % and approximately 0.04 % of the power at the standard noise on time scales of 3 seconds. The minimal noise indicates that relative calibration will yield sub-percent accuracy using auto spectra reported by each autonomous station. In the future, outright calibration will be extracted from the contrast of auto spectra with the co-located and thoroughly calibrated PRI^ZM or Global Sky Model. Figure 5.3 shows the cross-spectra phases binned in nearby sidereal time as a subjective representation of the sky signal repeatability on tiny scales.

In this plot, about 372 hours of data are averaged, and no RFI extraction has been carried out. The high signal-to-noise fringe pattern, which is noticeable even marginally beneath ~ 10 MHz, shows the verification of an idea for extending the ALBATROS array.

Due to COVID-19 restriction and limited accessibility to the island, the data could not be retrieved from the single autonomous station pathfinder on Marion discussed in §3.3; however, verification of the solar power system has effectively met the antenna station’s power requirements. Because of the unavailability of data from Marion, baseband writing has been demonstrated by setting up a single-element pathfinder station at the McGill Arctic Research Station (MARS; 79°26'N, 90°46'W) Axel Heiberg Island, Nunavut, in July 2019. The RF signal chain shown in Figure 3.9 is similar to the MARS installation; although a solar

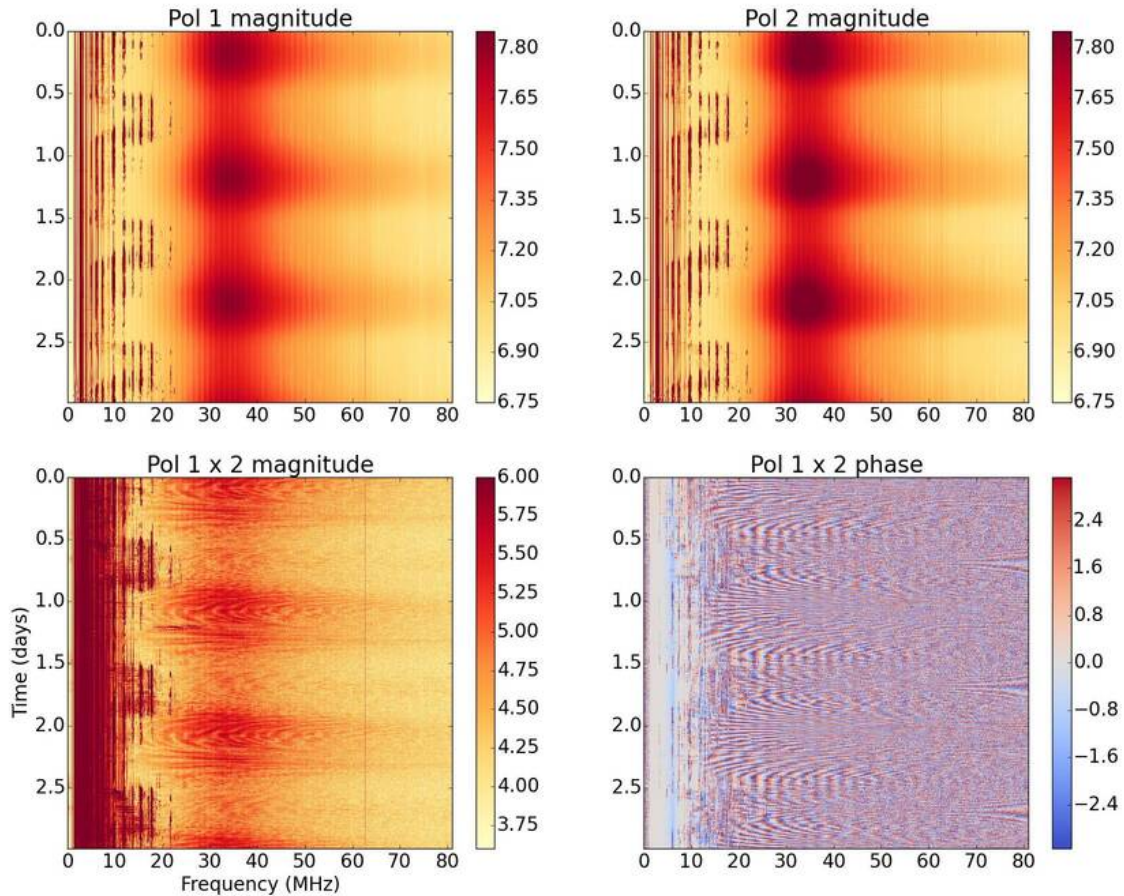


Figure 5.1: Spectra from a two-element ALBATROS pathfinder co-aligned polarization pair, shown as a frequency and time function. In the top and bottom rows, the auto- and cross-spectra are shown, respectively. The spectrum magnitudes are in uncalibrated ADC units on a logarithmic scale, and the amplitude of the cross-spectrum is around two orders of magnitude fainter than the auto spectra. The phase of the cross-spectrum can be seen in radians. The Galaxy's repeatable structure is evident in all plots over the 3-day time scale.

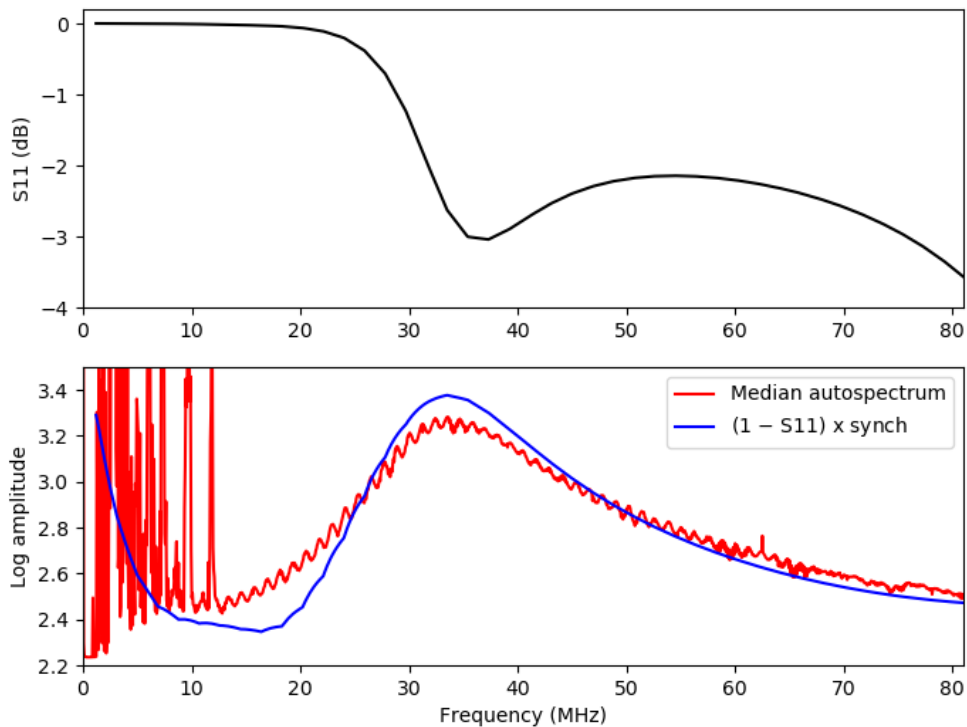


Figure 5.2: Top: LWA antenna simulated S11, demonstrating the steep loss of signal below ~ 30 MHz. Bottom panel: for one of the polarization in the two-element ALBATROS pathfinder, the median uncalibrated auto spectrum compared to the crude sky signal estimate provided by the product $(1-S11)$ with the product spectrum of nominal synchrotrons. Qualitatively, this simple model shows that the reduction in the antenna response is primarily responsible for auto spectrum power below ~ 30 MHz.

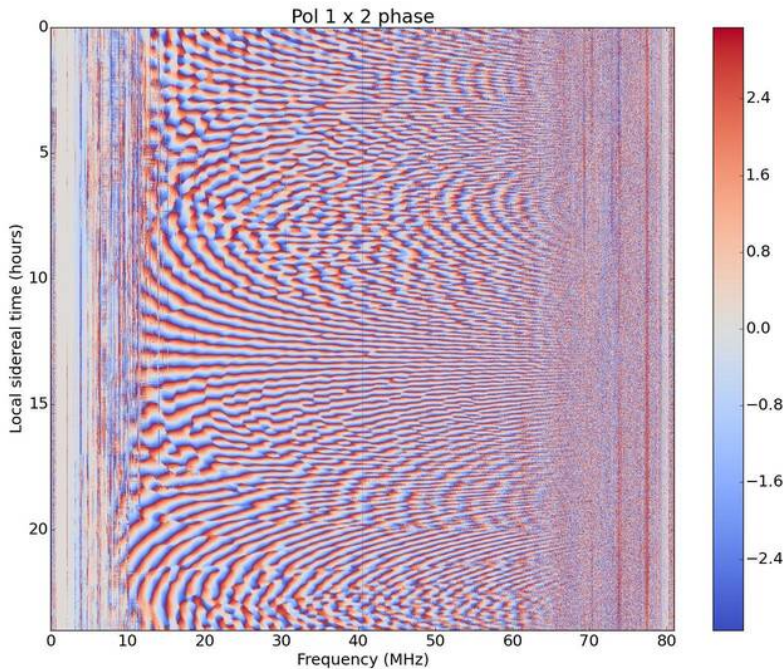


Figure 5.3: Phases from the cross-correlation in the two-element ALBATROS pathfinder between two co-aligned polarizations. There are approximately 372 hours of data displayed here, binned in local sidereal time, and radians are the color stretch.

power system was not used, instead manually charged batteries were used to supply power. The MARS RFI environment is much noisier than that of Marion Island. The ionospheric plasma cutoff frequency is higher than the average cutoff displayed in the Marion data because the data was taken during the peak of the Arctic summer. The MARS installation is appropriate for demonstrating baseband data writing, regardless of the distinct layout and RFI environment.

Short chunks of baseband data that have been collected at different times over two adjoining frequency windows are displayed, 5.3 MHz to 12.6 MHz and 12.6 MHz to 20 MHz. In order to maintain auto spectrum data, the baseband data was registered with 4-bit quantization, which is not obtainable with 1-bit quantization. The one polarization auto spectra from the ALBATROS single-element pathfinder station that was set-up at MARS is shown in Figure 5.4, looking at the aggregated spectra that are directly registered by the SNAP board versus the spectra determined from baseband data. Altogether, the waterfall plots have the same 61-kHz frequency resolution, as defined by the spectrum resolution measured by the SNAP board. A logarithmic scale is shown in the waterfall plots to demonstrate the qualitative agreement for bright and faint spectral characteristics between the directly accumulated and baseband spectra. In order to demonstrate variations in the striking RFI characteristics that immerse the baseband data, the bottommost panels display the time-averaged spectra on a linear scale. Except where major immersion is present, the portion of baseband data with values at the 4-bit extrema is over-plotted with spectra. There is general consistency between the directly accumulated and baseband spectra. Figure 5.5 shows waterfall phase plots calculated from the cross-correlation between two orthogonal polarizations of the ALBATROS pathfinder at MARS, looking at the directly accumu-

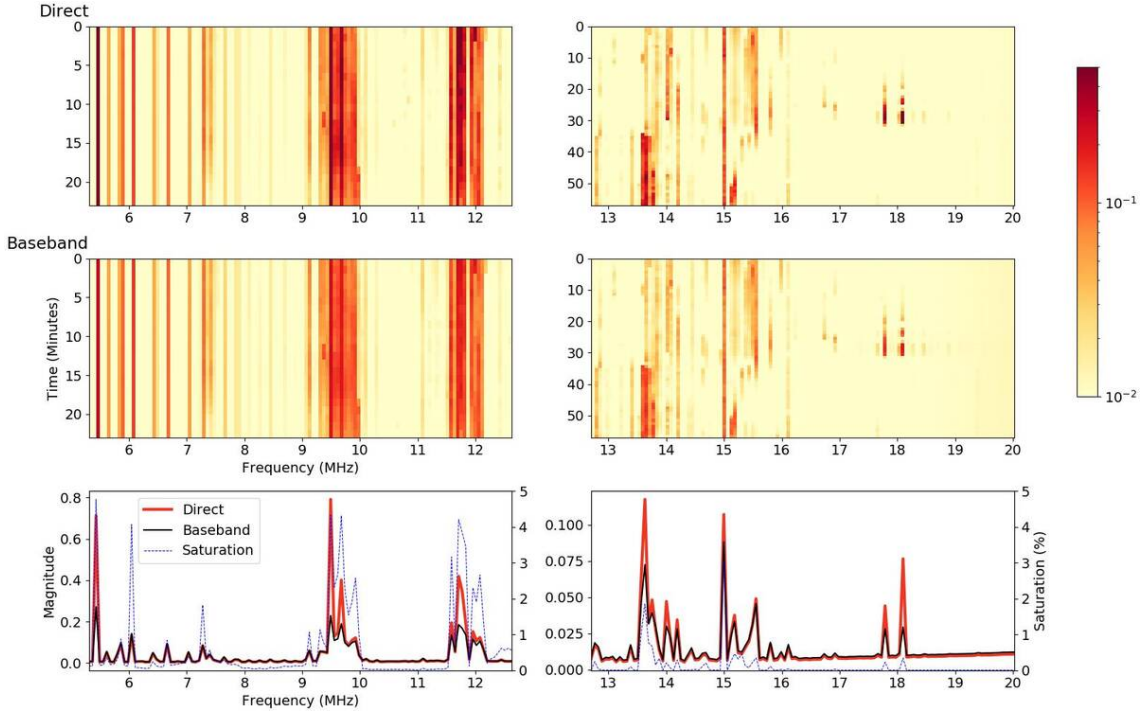


Figure 5.4: Autospectra from the ALBATROS pathfinder at MARS for one polarization. The top row shows spectra directly accumulated by the SNAP board, and the middle row displays spectra with 4-bit quantization computed from baseband data. The two frequency windows are registered at two different periods, 5.3-12.6 MHz and 12.6-20.0 MHz, and both plots are displayed at a 61-kHz resolution.

lated and baseband data. Qualitatively, both sets of reported data concur, down to minor variations induced by the 4-bit quantization.

5.1 Conclusion and Future Outlook

The design of ALBATROS a new interferometer that will image the radio sky at ~ 30 MHz using an array of autonomous antenna stations installed on Marion Island, has been presented. A clear demonstration of the repeatable sky signal visible from Marion down to $\lesssim 10$ MHz without data processing or cutting, with a two-element, directly correlated pathfinder. The first autonomous prototype for ALBATROS powered solar panels have been constructed, and the electronics and database recording software have been successfully tested.

There are plans to improve the design of the future ALBATROS stations to be deployed in the coastal huts of Marion, with the evidence of the concept shown in the pathfinder instruments presented here. Currently, the LWA and FEE antennas are not designed for the lowest ALBATROS frequency observation, and potential antenna and FEE design modifications are being explored to enhance the low-frequency response of the calibration circuitry construction. Since future ALBATROS stations would be located farther away from the base and will be more challenging to access regularly, to store baseband data over extended periods, each station will require larger total disk space. A specially made low-power hard disk drive bank is being developed with > 100 TB total capacity, and a USB

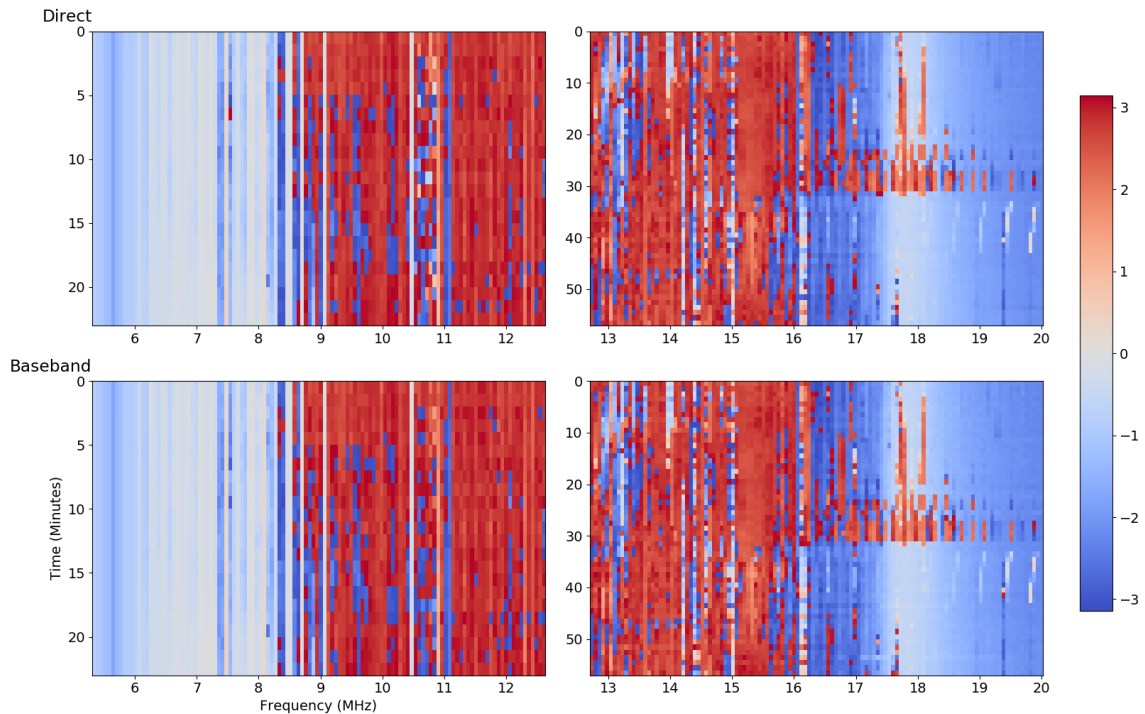


Figure 5.5: Cross-correlation phases between two orthogonal polarizations from the ALBATROS pathfinder at MARS. The top row shows cross-spectrum phases that are directly accumulated by the SNAP board, and the bottom row shows phases with 4-bit quantization computed from baseband results. The two frequency windows, 5.3 MHz to 12.6 MHz and 12.6 MHz to 20 MHz are registered at two different times, and all 61-kHz resolution waterfall plots are shown.

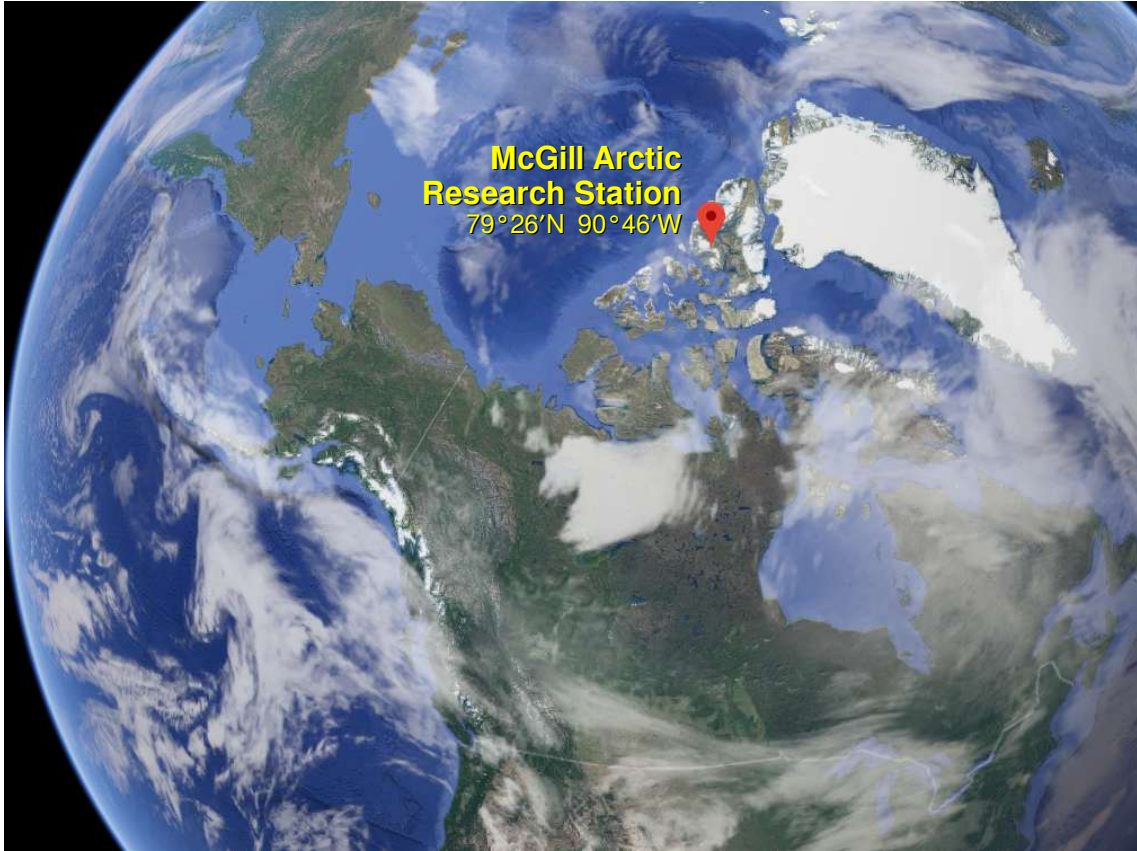


Figure 5.6: The world map showing the location of MARS, where the ALBATROS will be viewing the Northern hemisphere sky.

multiplexer will be used to select and power only one hard drive at a time. The autonomous pathfinder of the station presented uses solar panels to charge the batteries and, as a future alternative for potential stations, the use of small wind turbines is explored. To compute time-domain data from the recorded channelized baseband, analysis tools are being built by inverting the polyphase filter bank while minimizing quantization and saturation artifacts.

A proposal for building a second ALBATROS array at MARS shown in Figure 5.6 in the high Arctic is being studied in addition to Marion Island. In July 2019, a single pathfinder antenna was mounted as defined in §5 and observed for about three weeks to evaluate the RFI environment and ionospheric conditions. When fully operational, Marion and MARS ALBATROS will have new views across both hemispheres of the low-frequency sky.

The PRI^ZM experiment, which was the first radio astronomy project in Marion Island, was discussed, and the revision of the subsystems was presented. The new FSE was designed, and further modifications are still going to be employed. The SSE enclosure was successfully designed, fabricated and the enclosure parts were fitted together. The new switch control circuit design was successful, and it fitted the stacked layout on top of the RPi. All the PRI^ZM modifications are still going to be employed on the next Marion voyage, hopefully in April 2021.

Bibliography

H. C. Chiang, T. Dyson, E. Egan, S. Eyono, N. Ghazi, J. Hickish, J. M. Jauregui-Garcia, V. Manukha, T. Moso, J. Peterson, L. Philip, J. L. Sievers, and S. Tartakovsky. The Array of Long Baseline Antennas for Taking Radio Observations from the Sub-Antarctic. *arXiv e-prints*, art. arXiv:2008.12208, August 2020.

T. Dyson, H. C. Chiang, E. Egan, N. Ghazi, T. Menard, R. A. Monsalve, T. Moso, J. Peterson, J. L. Sievers, and S. Tartakovsky. Radio-Frequency Interference at the McGill Arctic Research Station. *arXiv e-prints*, art. arXiv:2012.06521, December 2020.

Turner M. S Kolb E. W. *The Early Universe*. Frontiers in Physics, v. 69. Addison-Wesley, 1988. ISBN 0201116030,9780201116038,0201626748,9780201626742. URL <http://gen.lib.rus.ec/book/index.php?md5=9EF28F934B0B80E2FE7A6921BEFA4D4E>.

Sheila Rabin. Nicolaus Copernicus. In Edward N. Zalta, editor, *The Stanford Encyclopedia of Philosophy*. Metaphysics Research Lab, Stanford University, fall 2019 edition, 2019.

Nick Kanas. *European cosmology*. In: Star Maps. Springer Praxis Books. Springer, New York, NY, 2012. ISBN 978-1-4614-0917-5. URL https://doi.org/10.1007/978-1-4614-0917-5_3.

M.J. Crowe. *Theories of the World from Antiquity to the Copernican Revolution: Second Revised Edition*. Dover Publications, 2013. ISBN 9780486315591. URL <https://books.google.co.za/books?id=gfzDAGAAQBAJ>.

E. P. Hubble. Extragalactic nebulae. *Astrophysical Journal*, 64:321–369, December 1926. doi: 10.1086/143018.

A. A. Penzias and R. W. Wilson. A Measurement of Excess Antenna Temperature at 4080 Mc/s. *Astrophysical Journal*, 142:419–421, July 1965. doi: 10.1086/148307.

P. J. Peebles and B. Ratra. The cosmological constant and dark energy. *Reviews of Modern Physics*, 75:559–606, April 2003. doi: 10.1103/RevModPhys.75.559.

E. Hubble. A Relation between Distance and Radial Velocity among Extra-Galactic Nebulae. *Proceedings of the National Academy of Science*, 15:168–173, March 1929. doi: 10.1073/pnas.15.3.168.

A. G. Riess, A. V. Filippenko, P. Challis, A. Clocchiatti, A. Diercks, P. M. Garnavich, R. L. Gilliland, C. J. Hogan, S. Jha, R. P. Kirshner, B. Leibundgut, M. M.

- Phillips, D. Reiss, B. P. Schmidt, R. A. Schommer, R. C. Smith, J. Spyromilio, C. Stubbs, N. B. Suntzeff, and J. Tonry. Observational Evidence from Supernovae for an Accelerating Universe and a Cosmological Constant. *Astronomical Journal*, 116:1009–1038, September 1998. doi: 10.1086/300499.
- S. Perlmutter, G. Aldering, G. Goldhaber, R. A. Knop, P. Nugent, P. G. Castro, S. Deustua, S. Fabbro, A. Goobar, D. E. Groom, I. M. Hook, A. G. Kim, M. Y. Kim, J. C. Lee, N. J. Nunes, R. Pain, C. R. Pennypacker, R. Quimby, C. Lidman, R. S. Ellis, M. Irwin, R. G. McMahon, P. Ruiz-Lapuente, N. Walton, B. Schaefer, B. J. Boyle, A. V. Filippenko, T. Matheson, A. S. Fruchter, N. Panagia, H. J. M. Newberg, W. J. Couch, and T. S. C. Project. Measurements of Ω and Λ from 42 High-Redshift Supernovae. *Astrophysical Journal*, 517:565–586, June 1999. doi: 10.1086/307221.
- J. A. Frieman, M. S. Turner, and D. Huterer. Dark Energy and the Accelerating Universe. *Annual Review of Astronomy and Astrophysics*, 46:385–432, September 2008. doi: 10.1146/annurev.astro.46.060407.145243.
- Alan H. Guth. Inflationary universe: A possible solution to the horizon and flatness problems. *Physical Review D*, 23(2):347–356, January 1981. doi: 10.1103/PhysRevD.23.347.
- J. Lazio, A. Loeb, J. Aguirre, J. Bowman, J. Burns, O. Dore, S. Furlanetto, C. Lonsdale, A. Parsons, and J. Pober. Probing the Dark Ages and Cosmic Dawn with Neutral Hydrogen. *Science*, 2016. URL https://cor.gsfc.nasa.gov/copag/probe-study/COPAG_Probe_DarkAges-CosmicDawn-v3.pdf.
- A. Loeb and M. Zaldarriaga. Measuring the Small-Scale Power Spectrum of Cosmic Density Fluctuations through 21cm Tomography Prior to the Epoch of Structure Formation. *Physical Review Letters*, 92(21):211301, May 2004. doi: 10.1103/PhysRevLett.92.211301.
- M. Deng, D. Campbell-Wilson, and for the CHIME Collaboration. The cloverleaf antenna: A compact wide-bandwidth dual-polarization feed for CHIME. *ArXiv e-prints*, August 2017.
- Jack O. Burns, J. Lazio, S. Bale, J. Bowman, R. Bradley, C. Carilli, S. Furlanetto, G. Harker, A. Loeb, and J. Pritchard. Probing the first stars and black holes in the early Universe with the Dark Ages Radio Explorer (DARE). *Advances in Space Research*, 49(3):433–450, February 2012. doi: 10.1016/j.asr.2011.10.014.
- Jonathan R. Pritchard and Abraham Loeb. 21 cm cosmology in the 21st century. *Reports on Progress in Physics*, 75(8):086901, August 2012. doi: 10.1088/0034-4885/75/8/086901.
- A. Liu, J. R. Pritchard, M. Tegmark, and A. Loeb. Global 21 cm signal experiments: A designer’s guide. *Physical Review D*, 87(4):043002, February 2013. doi: 10.1103/PhysRevD.87.043002.
- J. C. Pober, A. Liu, J. S. Dillon, J. E. Aguirre, J. D. Bowman, R. F. Bradley, C. L. Carilli, D. R. DeBoer, J. N. Hewitt, D. C. Jacobs, M. McQuinn, M. F. Morales, A. R. Parsons, M. Tegmark, and D. J. Werthimer. What Next-generation 21 cm

Power Spectrum Measurements can Teach us About the Epoch of Reionization. *Astrophysical Journal*, 782:66, February 2014. doi: 10.1088/0004-637X/782/2/66.

Douglas C. Giancoli. *Physics for Scientists and Engineers with Modern Physics (4th Edition)* 1, 2, 3. Pearson Prentice Hall, 4th edition edition, 2008. ISBN 0131495089,9780131495081,0321542142,9780321542144. URL <http://gen.lib.rus.ec/book/index.php?md5=867E74BB25C30D895AC60E0EB937298A>.

L. Liu and C. Chronopoulos. The Hydrogen 21-cm Line and Its Applications to Radio Astrophysics. *Astrophysics*, March 2008. URL <http://web.mit.edu/lululiu/Public/8.14/21cm/21cm.pdf>.

L. Koopmans, J. Pritchard, G. Mellema, J. Aguirre, K. Ahn, R. Barkana, I. van Beemel, G. Bernardi, A. Bonaldi, F. Briggs, A. G. de Bruyn, T. C. Chang, E. Chapman, X. Chen, B. Ciardi, P. Dayal, A. Ferrara, A. Fialkov, F. Fiore, K. Ichiki, I. T. Illiev, S. Inoue, V. Jelic, M. Jones, J. Lazio, U. Maio, S. Majumdar, K. J. Mack, A. Mesinger, M. F. Morales, A. Parsons, U. L. Pen, M. Santos, R. Schneider, B. Semelin, R. S. de Souza, R. Subrahmanyam, T. Takeuchi, H. Vedantham, J. Wagg, R. Webster, S. Wyithe, K. K. Datta, and C. Trott. The Cosmic Dawn and Epoch of Reionisation with SKA. In *Advancing Astrophysics with the Square Kilometre Array (AASKA14)*, page 1, April 2015.

Steven R. Furlanetto, S. Peng Oh, and Frank H. Briggs. Cosmology at low frequencies: The 21 cm transition and the high-redshift Universe. *Physical Reports*, 433(4-6):181–301, October 2006. doi: 10.1016/j.physrep.2006.08.002.

Dayton L. Jones, T. Joseph W. Lazio, and Jack O. Burns. Dark Ages Radio Explorer Mission: Probing the Cosmic Dawn. *arXiv e-prints*, art. arXiv:1412.2096, December 2014.

Jordi Miralda-Escudé. The Dark Age of the Universe. *Science*, 300(5627):1904–1909, June 2003. doi: 10.1126/science.1085325.

Qi-Zhi Huang, Feng-Quan Wu, Reza Ansari, and Xuelei Chen. Extracting 21 cm signal by frequency and angular filtering. *Research in Astronomy and Astrophysics*, 18(9):114, August 2018. doi: 10.1088/1674-4527/18/9/114.

V. Jelić, S. Zaroubi, P. Labropoulos, R. M. Thomas, G. Bernardi, M. A. Brentjens, A. G. de Bruyn, B. Ciardi, G. Harker, L. V. E. Koopmans, V. N. Pandey, J. Schaye, and S. Yatawatta. Foreground simulations for the LOFAR-epoch of reionization experiment. *Monthly Notices of the Royal Astronomical Society*, 389(3):1319–1335, September 2008. doi: 10.1111/j.1365-2966.2008.13634.x.

Adrian Liu and J. Richard Shaw. Data Analysis for Precision 21 cm Cosmology. *Proceedings of the Astronomical Society of the Pacific*, 132(1012):062001, June 2020. doi: 10.1088/1538-3873/ab5bfd.

A. R. Neben, R. F. Bradley, J. N. Hewitt, G. Bernardi, J. D. Bowman, F. Briggs, R. J. Cappallo, A. A. Deshpande, R. Goeke, L. J. Greenhill, B. J. Hazelton, M. Johnston-Hollitt, D. L. Kaplan, C. J. Lonsdale, S. R. McWhirter, D. A. Mitchell, M. F. Morales, E. Morgan, D. Oberoi, S. M. Ord, T. Prabu, N. Udaya

Shankar, K. S. Srivani, R. Subrahmanyam, S. J. Tingay, R. B. Wayth, R. L. Webster, A. Williams, and C. L. Williams. Measuring phased-array antenna beam-patterns with high dynamic range for the Murchison Widefield Array using 137 MHz ORBCOMM satellites. *Radio Science*, 50(7):614–629, July 2015. doi: 10.1002/2015RS005678.

J. L. B. Line, B. McKinley, J. Rasti, M. Bhardwaj, R. B. Wayth, R. L. Webster, D. Ung, D. Emrich, L. Horsley, A. Beardsley, B. Crosse, T. M. O. Franzen, B. M. Gaensler, M. Johnston-Hollitt, D. L. Kaplan, D. Kenney, M. F. Morales, D. Pallot, K. Steele, S. J. Tingay, C. M. Trott, M. Walker, A. Williams, and C. Wu. In situ measurement of MWA primary beam variation using ORBCOMM. *Publications of the Astronomical Society of Australia*, 35:45, December 2018. doi: 10.1017/pasa.2018.30.

Xuelei Chen, Jack Burns, Leon Koopmans, Hanna Rothkaehl, Joseph Silk, Ji Wu, Albert-Jan Boonstra, Baptiste Cecconi, Cynthia H. Chiang, Linjie Chen, Li Deng, Maurizio Falanga, Heino Falcke, Quanlin Fan, Guangyou Fang, Anastasia Fialkov, Leonid Gurvits, Yicai Ji, Justin C. Kasper, Kejia Li, Yi Mao, Benjamin McKinley, Raul Monsalve, Jeffery B. Peterson, Jinsong Ping, Ravi Subrahmanyam, Harish Vedantham, Marc Klein Wolt, Fengquan Wu, Yidong Xu, Jingye Yan, and Bin Yue. Discovering the Sky at the Longest Wavelengths with Small Satellite Constellations. *arXiv e-prints*, art. arXiv:1907.10853, July 2019.

Leon Koopmans, Rennan Barkana, Mark Bentum, Gianni Bernardi, Albert-Jan Boonstra, Judd Bowman, Jack Burns, Xuelei Chen, Abhirup Datta, Heino Falcke, Anastasia Fialkov, Bharat Gehlot, Leonid Gurvits, Vibor Jelić, Marc Klein-Wolt, Léon Koopmans, Joseph Lazio, Daan Meerburg, Garrelt Mellema, Florent Mertens, Andrei Mesinger, André Offringa, Jonathan Pritchard, Benoit Semelin, Ravi Subrahmanyam, Joseph Silk, Cathryn Trott, Harish Vedantham, Licia Verde, Saleem Zaroubi, and Philippe Zarka. Peering into the Dark (Ages) with Low-Frequency Space Interferometers. *arXiv e-prints*, art. arXiv:1908.04296, August 2019.

Raul A. Monsalve, Alan E. E. Rogers, Judd D. Bowman, and Thomas J. Mozdzen. Calibration of the EDGES High-band Receiver to Observe the Global 21 cm Signature from the Epoch of Reionization. *Astrophysical Journal*, 835(1):49, January 2017. doi: 10.3847/1538-4357/835/1/49.

Judd D. Bowman, Alan E. E. Rogers, Raul A. Monsalve, Thomas J. Mozdzen, and Nivedita Mahesh. An absorption profile centred at 78 megahertz in the sky-averaged spectrum. *Nature Journal*, 555(7694):67–70, March 2018. doi: 10.1038/nature25792.

Rennan Barkana. Possible interaction between baryons and dark-matter particles revealed by the first stars. *Nature Journal*, 555(7694):71–74, March 2018. doi: 10.1038/nature25791.

Rennan Barkana, Nadav Joseph Outmezguine, Diego Redigolo, and Tomer Volansky. Strong constraints on light dark matter interpretation of the edges signal. *Phys. Rev. D*, 98:103005, Nov 2018. doi: 10.1103/PhysRevD.98.103005. URL <https://link.aps.org/doi/10.1103/PhysRevD.98.103005>.

Bang D. Nhan, David D. Bordenave, Richard F. Bradley, Jack O. Burns, Keith Tauscher, David Rapetti, and Patricia J. Klima. Assessment of the Projection-induced Polarimetry Technique for Constraining the Foreground Spectrum in Global 21 cm Cosmology. *Astrophysical Journal*, 883(2):126, October 2019. doi: 10.3847/1538-4357/ab391b.

G. B. Taylor, S. W. Ellingson, N. E. Kassim, J. Craig, J. Dowell, C. N. Wolfe, J. Hartman, G. Bernardi, T. Clarke, A. Cohen, N. P. Dalal, W. C. Erickson, B. Hicks, L. J. Greenhill, B. Jacoby, W. Lane, J. Lazio, D. Mitchell, R. Navarro, S. M. Ord, Y. Pihlström, E. Polisensky, P. S. Ray, L. J. Rickard, F. K. Schinzel, H. Schmitt, E. Sigman, M. Soriano, K. P. Stewart, K. Stovall, S. Tremblay, D. Wang, K. W. Weiler, S. White, and D. L. Wood. First Light for the First Station of the Long Wavelength Array. *Journal of Astronomical Instrumentation*, 1:1250004-284, December 2012. doi: 10.1142/S2251171712500043.

D. C. Price, L. J. Greenhill, A. Fialkov, G. Bernardi, H. Garsden, B. R. Barsdell, J. Kocz, M. M. Anderson, S. A. Bourke, J. Craig, M. R. Dexter, J. Dowell, M. W. Eastwood, T. Eftekhar, S. W. Ellingson, G. Hallinan, J. M. Hartman, R. Kimberk, T. Joseph W. Lazio, S. Leiker, D. MacMahon, R. Monroe, F. Schinzel, G. B. Taylor, E. Tong, D. Werthimer, and D. P. Woody. Design and characterization of the Large-aperture Experiment to Detect the Dark Age (LEDA) radiometer systems. *Monthly Notices of the Royal Astronomical Society*, 478(3):4193–4213, August 2018. doi: 10.1093/mnras/sty1244.

Raúl Monsalve, Ricardo Bustos, H Chiang, Jonathan Sievers, Nithyanandan Thyagarajan, Patricio Mena, Mauricio Díaz, Christian Bye, Oscar Restrepo, and Matheus Pessoa. Mist: A new radio experiment to detect the first stars in the universe.

L. Philip, Z. Abdurashidova, H. C. Chiang, N. Ghazi, A. Gumba, H. M. Heilgendorff, J. M. Jáuregui-García, K. Malepe, C. D. Nunhokee, J. Peterson, J. L. Sievers, V. Simes, and R. Spann. Probing Radio Intensity at High-Z from Marion: 2017 Instrument. *Journal of Astronomical Instrumentation*, 8(2):1950004, January 2019. doi: 10.1142/S2251171719500041.

E. de Lera Acedo. Reach: Radio experiment for the analysis of cosmic hydrogen. In *2019 International Conference on Electromagnetics in Advanced Applications (ICEAA)*, pages 0626–0629, 2019. doi: 10.1109/ICEAA.2019.8879199.

Nipanjana Patra, Ravi Subrahmanyam, A. Raghunathan, and N. Udaya Shankar. SARAS: a precision system for measurement of the cosmic radio background and signatures from the epoch of reionization. *Experimental Astronomy*, 36(1-2): 319–370, August 2013. doi: 10.1007/s10686-013-9336-3.

D. Fisher Miller. *Basics of Radio Astronomy for the Goldstone-Apple Valley Radio Telescope*. Jet Propulsion Laboratory Mission Execution and Automation Section Customer Integration Services Group, 1998. ISBN JPL D-13835. URL https://www2.jpl.nasa.gov/radioastronomy/radioastronomy_all.pdf.

John D. Kraus. *Radio Astronomy*. Powell, Ohio: Cygnus - Quasar Books, Durham, 2nd edition edition, 1986.

- G. Reber. A Play Entitled the Beginning of Radio Astronomy. *Journal of the Royal Astronomical Society of Canada*, 82:93, June 1988.
- G. Reber. Cosmic Static. volume 30, pages 367 – 378, August 1942. doi: 10.1109/JRPROC.1942.231700. URL <https://ieeexplore.ieee.org/abstract/document/1694527/references#references>.
- B. C. Hicks, N. Paravastu-Dalal, K. P. Stewart, W. C. Erickson, P. S. Ray, N. E. Kassim, S. Burns, T. Clarke, H. Schmitt, J. Craig, J. Hartman, and K. W. Weiler. A Wide-Band, Active Antenna System for Long Wavelength Radio Astronomy. *Proceedings of the Astronomical Society of the Pacific*, 124:1090, October 2012. doi: 10.1086/668121.
- A. C. B. Lovell. The investigation of the universe by radio astronomy: Synopsis. *Notes and Records of the Royal Society of London*, 16(1):65–68, 1961. ISSN 00359149. URL <http://www.jstor.org/stable/530765>.
- J. K. Alexander, M. L. Kaiser, J. C. Novaco, F. R. Grena, and R. R. Weber. Scientific instrumentation of the Radio-Astronomy-Explorer-2 satellite. *Astronomy and Astrophysics*, 40:365–371, May 1975.
- M. W. Eastwood, M. M. Anderson, R. M. Monroe, G. Hallinan, B. R. Barsdell, S. A. Bourke, M. A. Clark, S. W. Ellingson, J. Dowell, H. Garsden, L. J. Greenhill, J. M. Hartman, J. Kocz, T. J. W. Lazio, D. C. Price, F. K. Schinzel, G. B. Taylor, H. K. Vedantham, Y. Wang, and D. P. Woody. The Radio Sky at Meter Wavelengths: m-mode Analysis Imaging with the OVRO-LWA. *Astronomical Journal*, 156:32, July 2018. doi: 10.3847/1538-3881/aac721.
- R. S. Roger, C. H. Costain, T. L. Landecker, and C. M. Swerdflyk. The radio emission from the Galaxy at 22 MHz. *Astronomy and Astrophysics Supplements*, 137: 7–19, May 1999. doi: 10.1051/aas:1999239.
- J. L. Caswell. A map of the northern sky at 10 MHz. *Monthly Notices of the Royal Astronomical Society*, 177:601–616, December 1976. doi: 10.1093/mnras/177.3.601.
- Prince Edward Islands. https://en.wikipedia.org/wiki/Prince_Edward_Islands, 2007. [Online; accessed 20-January-2021].
- J. M. Wislez. Forward scattering of radio waves off meteor trails. In *Proceedings of the International Meteor Conference, 14th IMC, Brandenburg, Germany, 1995*, pages 99–117, January 1996.
- D. Bilitza. Iri the international standard for the ionosphere. *Advances in Radio Science*, 16:1–11, 2018. doi: 10.5194/ars-16-1-2018. URL <https://ars.copernicus.org/articles/16/1/2018/>.
- Prantika Bhowmik and Dibyendu Nandy. Prediction of the strength and timing of sunspot cycle 25 reveal decadal-scale space environmental conditions. *Nature Communications*, 9:5209, December 2018. doi: 10.1038/s41467-018-07690-0.

- S. Ellingson and W. T. Kramer. Designing a Sky-Noise-Limited Receiver for LWA. *Long Wavelength Array Memo* (28), 2004. URL <https://www.faculty.ece.vt.edu/swe/lwa/memo/lwa0028.pdf>.
- S. W. Ellingson. Receivers for Low-Frequency Radio Astronomy. *Long Wavelength Array Memo* (27), 2005. URL <https://www.faculty.ece.vt.edu/swe/lwa/memo/lwa0027.pdf>.
- Steven Ellingson, Tracy Clarke, Aaron Cohen, Joseph Craig, Nurfatin Kassim, Y. Pihlström, Lee Rickard, and Gregory Taylor. The long wavelength array. *Proceedings of the IEEE*, 97:1421 – 1430, 09 2009. doi: 10.1109/JPROC.2009.2015683.
- P. S. Ray, S. W. Ellingson, R. Fisher, N. E. Kassim, L. J. Rickard, and T. Clarke. A Strawman Design for the Long Wavelength Array Stations. *Long Wavelength Array Memo* (35), 2006. URL <https://www.faculty.ece.vt.edu/swe/lwa/memo/lwa0035.pdf>.
- Jack Hickish, Zuhra Abdurashidova, Zaki Ali, Kaushal D. Buch, Sandeep C. Chaudhari, Hong Chen, Matthew Dexter, Rachel Simone Domagalski, John Ford, Griffin Foster, David George, Joe Greenberg, Lincoln Greenhill, Adam Isaacson, Homin Jiang, Glenn Jones, Francois Kapp, Henno Kriel, Rich Lacasse, Andrew Lutomirski, David MacMahon, Jason Manley, Andrew Martens, Randy McCullough, Mekhala V. Muley, Wesley New, Aaron Parsons, Daniel C. Price, Rurik A. Primiani, Jason Ray, Andrew Siemion, Vereesé van Tonder, Laura Vertatschitsch, Mark Wagner, Jonathan Weintraub, and Dan Werthimer. A Decade of Developing Radio-Astronomy Instrumentation using CASPER Open-Source Technology. *Journal of Astronomical Instrumentation*, 5(4):1641001-12, December 2016. doi: 10.1142/S2251171716410014.
- J. M. Jáuregui-García, J. B. Peterson, E. Castillo-Domínguez, and T. C. Voytek. Hibiscus, a broadband antenna with matching impedance and uniform radiation pattern. In *2017 IEEE International Symposium on Antennas and Propagation USNC/URSI National Radio Science Meeting*, pages 697–698, 2017. doi: 10.1109/APUSNCURSINRSM.2017.8072391.
- T. C. Voytek, A. Natarajan, J. M. Jáuregui García, J. B. Peterson, and O. López-Cruz. Probing the Dark Ages at $z \sim 20$: The SCI-HI 21 cm All-sky Spectrum Experiment. *The Astrophysical Journal Letters*, 782:L9, February 2014. doi: 10.1088/2041-8205/782/1/L9.